NOTE: This manuscript is **not** peer reviewed and has been submitted to Geostandards and Geoanalytical Research for consideration of publication.

Improved LA-Q-ICP-MS U-Pb Zircon Age Estimates for Young (< 10 Ma) Zircons & Quantification of Bias in CL Guided Spot Selection

Chuck Lewis[1*], Adam Kent[1], Chris Russo[1], Shanaka de Silva[1]

[1]Oregon State University; College of Earth, Ocean, and Atmospheric Sciences (CEOAS);

104 CEOAS Admin Bldg. Corvallis, OR 97331

*Corresponding Author: lewisc2@oregonstate.edu

Abstract

We present a new approach to reducing U-Pb data from zircons obtained by laser ablation-quadrupole-inductively coupled plasma-mass spectrometry (LA-Q-ICP-MS), with emphasis on young (< 10 Ma) zircons. In young zircons the ^{207}Pb yield is extremely low, generating a relatively high abundance of zero values during analyses. This impacts the use of $^{207}Pb/^{206}Pb$ in application of Tera-Wasserburg Concordia, widely used to assess discordance and correct for common Pb. To improve estimates of ^{207}Pb and $^{207}Pb/^{206}Pb$ in zircon we explore the use of two distributions that deal with zero values explicitly: the Zero-Inflated Poisson (ZIP) and the Zero-Truncated Normal (ZTN). From this we develop an approach to apply ^{207}Pb and $^{207}Pb/^{206}Pb$ distributions that are appropriately bound at zero by application of the ZIP, which produces smaller overall uncertainties, but slightly higher discordance. This approach improves precision relative to assuming a Gaussian distribution while producing ratios and zircon ages that are within error despite the small increase in discordance (~ 0.5% under optimized analytical conditions).

Improved precision on LA-Q-ICP-MS zircons ages facilitates more rigorous cross-method comparison of ages gathered by LA-multicollector (MC)-ICP-MS in this study as well as previously collected Secondary Ion Mass Spectrometry (SIMS) ages on the same rocks. Both sets of LA ages are systematically older than SIMS ages, which are interpreted as higher incidence of older antecrystic and xenocrystic populations in the LA datasets. Qualitative analysis of CL-images suggested that this bias is due to targeted spot-selection (i.e., avoidance of specific CL-textures in cores). Following through, quantitative bias methodology is applied to quantify age bias based on user-guided spot selection via CL-texture. Based on the bias found, we quantitatively corroborate the important point that interpretations of magmatic

systems using zircon U-Pb geochronology should account for any bias (conscious or unconscious) during spot selection.

Introduction

High sample throughput and availability make Laser Ablation-Inductively Coupled Plasma-Mass Spectrometry (LA-ICP-MS) a cost-effective technique to conduct U-Pb geochronology in zircons (Jackson et al., 2004). Many U-Pb zircon studies conducted via LA-ICP-MS use quadrupole mass analyzers (hereafter LA-Q-ICP-MS) due to their cost effectiveness, availability, and range of targetable masses in a single analytical session (i.e., simultaneous trace element collection) relative to other ICP-MS instruments capable of U-Pb geochronology (Kylander-Clark, 2017). However, quadrupole mass analyzers are also associated with lower overall ion transmission rates and in comparison to multicollector instruments also have a loss of counting efficiency as an artifact of sequential analysis and total duty cycle (i.e., Longerich et al., 1996) (**Table 1**). The lower count rates result in a loss of precision on measurements of U and Pb isotopes, and these issues are specifically exacerbated when analyzing young zircons (< ~10 Ma) due to lower abundance of radiogenic Pb isotopes. Analysis of ^{207}Pb (**Figure 1**) is particularly problematic. Low count rates for ^{207}Pb cause Gaussian statistics (the normal distribution) to be a poor descriptor for the ^{207}Pb/^{206}Pb ratio (Horstwood et al., 2016) **(Figure 2)** that should otherwise be applied to determine these quantities. Accurate measurements of ^{207}Pb/^{206}Pb ratios in young zircons are also required to implement the use of Tera-Wasserburg (TW-) Concordia methods to evaluate and correct for common Pb (Jackson et al., 2004; Košler and Sylvester, 2003), should accurate and reasonably precise measurement of ^{204}Pb be unattainable. Given this, an improved methodology for estimating the $^{207}Pb/^{206}Pb$ ratios offers many advantages.

Efforts to improve U-Pb geochronology for young zircons via LA-Q-ICP-MS are also desirable to promote broader access to higher quality geochronology and thus more impactful work (Ehrenberg and Mavros, 1995). Such data is specifically critical for understanding the behavior of young magmatic systems, which are frequently studied as part of volcanic hazard mitigation efforts (National Academies of Sciences, Engineering, and Medicine, 2020). Absolute uncertainties in zircon U-Pb ages are also smaller for younger systems and therefore have a greater chance of being comparable to or less than the timescales of consequential magmatic processes such as magma residence, remobilization, and differentiation (Gaynor et al., 2022; Kent and Cooper, 2018) and post-climactic volcanism and resurgence (Mucek et al., 2017). Although the general features of volcanic and magmatic activity in a region may be realized with higher absolute errors on older zircons (e.g., Tang et al., 2017) accurate descriptions of rates at which magmatic systems cool and differentiate, assemble, or recycle and recover themselves requires higher absolute precision – ideally on the order of 10’s of thousands of years (Miller et al., 2007; Mucek et al., 2017; Rivera et al., 2016; Schaen et al., 2021). In addition, use of a large number of analyses, forming an *age spectra* for a given sample may allow further characterization of magmatic processes if groups of individual ages can be assigned to specific zircon crystallization events (e.g. Weber et al., 2020). Minimizing absolute and relative uncertainties thus has the direct effect of revealing greater structure in age spectra.

In order to improve the estimates of ^{207}Pb and $^{207}Pb/^{206}Pb$ ratios measured for U-Pb geochronology of young zircons there are several statistical approaches that can be taken. Herein we explore two of the most promising methods: (i) the Zero-Inflated Poisson (ZIP) distribution, which explicitly accounts for the possibility that ions were not detected at a given pass of the detector despite their presence (i.e., zeros generated by low sensitivity) and that a zero may be generated by random variability when the true value of the $^{207}Pb/^{206}Pb$ ratio is extremely close to zero; and (ii) the Zero-Truncated Normal (ZTN), a distribution that allows for truncation of the normal distribution at zero (**Figure 1**). We show that application of both these approaches can improve uncertainties on measurements of $^{207}Pb/^{206}Pb$ and the estimated U-Pb age for young zircons, and ultimately develop a methodology based on the ZIP.

In concert with these statistical improvements, we directly compare LA-Q-ICP-MS ages to those collected with the more precise LA-MC-ICP-MS methodology as well as a previous study that utilized SIMS. This external comparison illuminates a bias between LA-ICP-MS datasets and SIMS. Inadvertent bias may arise from a number of sources, including the crystal selection process during mechanical mineral separation and picking (Sláma and Košler, 2012) and from spot selection during analysis (Dröllner et al., 2021; Malusà et al., 2013). Application of quantitative bias models shows the choice of spot selection based on CL-texture, particularly when coupled with the difference in analytical volumes between different analysis methods, may significantly alter interpretations of magmatic systems. We conclude that any preferential selection of mineral domains (e.g., cores vs rims; simple vs complex zoning) during *in-situ* analysis places bounds on the range of allowable interpretations.

Geologic Context of Samples

The analytical program that underpins this contribution was conducted as part of a study on the Chaxas complex, Northern Chile (Lewis et al., 2025). Inception of magmatism at the Chaxas complex is marked by a small rhyolitic eruption at 5.49 ± 0.15 Ma. Adjacent to the Chaxas edifice, the Puripicar ignimbrite (PPI; ≥ 500km^3 DRE) erupted at 4.18 ± 0.03 Ma, leaving behind a residual upper crustal magmatic system beneath what is now the modern volcanic arc (**Figure 4**). Shortly after eruption of the Puripicar Ignimbrite, the Embaucador Rhyolite (ER) (3.729 ± 0.017 Ma) erupted from the Chaxas edifice. Following this the Chaxas domes were emplaced and emanated block and ash flows that inundated the area around the domes (**Figure 4**) along with minor rhyolitic fallouts and pyroclastic flows for nearly three million years.

U-Pb zircon ages previously collected for the PPI via SIMS revealed a unimodal age distribution with no xenocrystic ages (Kern et al., 2016), despite the large volume and significant crustal assimilation implied by elevated $^{87}Sr/^{86}Sr$ ratios (Kay et al., 2010). Notably, assimilation in the region has been demonstrated to occur throughout the crust via MASH (Mixing, Assimilation, Storage, and Homogenization) processes in the lower (Hildreth and Moorbath, 1988) and middle crust (Burns et al., 2015; de Silva et al., 2006). Lack of xenocrysts ages in the PPI collected by SIMS (Kern et al., 2016) is therefore unexpected given the size of the ignimbrite and the clear radiogenic isotopic signature developed through crustal assimilation (de Silva, 1991, 1989). The lack of xenocrystic ages in the SIMS data set was interpreted to be due to resorption of assimilated zircon in the mid-crust followed by zircon saturation in the upper crust prior to eruption (Kern et al., 2016).

Methods

In this study we focus on zircons separated from PPI pumice sample from Kern et al. (2016) in addition to pumice from the ER and a block of the Middle Block and Ash flow (MBA) from the Chaxas Complex. Sample preparation protocol and LA-ICP-MS methodology are reported in **Table 2** according to essential data reporting protocol (Horstwood et al., 2016).

Sample Preparation and Cathodoluminescence (CL) Imaging

Sample Preparation: Pumice samples and blocks were crushed into chips on the order of 10’s of cm using an ASJ steel jaw crusher at Oregon State University (OSU). Chipped rocks were then ground to a coarse sand sized powder using an agate mortar and pestle. Rock powder was then passed through a series of sieves with mesh sizes of 1mm, 500μm, and 250μm. The size fraction ≤ 250 μm was collected in the catch sieve. A gold pan was then used to segregate the heavy mineral fraction from fines and light minerals in the smallest size fraction. Heavy mineral separates from this method included minerals less dense than zircon (i.e., pyroxene, some plagioclase). Zircon grains were then picked using a binocular microscope equipped with cross-polarizing lenses, such that bias in selection of zircon grains as a function of color was minimized. Grains were placed on double sided polyimide tape immediately upon picking to make an epoxy plug grain mount with Struers® epoxy resin and set in a drying oven at 40°C to cure. Grain mounts were polished using 1200 grit Si-C paper to expose the grains. Polishing was completed using 9μm, 3μm, and 1μm diamond laps. Grain mounts were sonicated after each polishing step for 15 minutes. After the final step grains were rinsed with methanol then DI in preparation for CL-imaging.

CL-Imaging: Prior to coating grain mounts Cu-tape was put on the surface of the epoxy grain mount (not in contact with grains) and wrapped to the stub on the bottom of the grain mount to ground any charging during CL-imaging. Grain mounts were coated with a thin AuPd coating. CL-images were gathered in high vacuum mode with a working distance of 10mm on the FEI Quanta 600F secondary electron microscope (SEM) with an ancillary Gatan® mini-CL at the Linus Pauling institute at OSU. High voltage was set to 15 kV and the spot size was set to 4.0 µm. Brightness and contrast setting on the CL-detector were held constant across samples. Following CL-imaging, samples were polished using 0.3µm aluminum polishing medium to remove the AuPd coat then cleaned prior to analysis using the procedure described above.

Analytical Equipment and Analysis

LA-ICP-MS analyses were conducted in the Keck Collaboratory at OSU using an Applied Spectra RESOlution-SE 193nm ArF Excimer Laser equipped with a Laurin Technic S155 two-volume sample cell. Isotope abundances were collected using either a ThermoFisher® i-CAP RQ quadrupole ICP-MS (denoted as LA-Q-ICP-MS) or a NuPlasma3 multicollector ICP-MS (denoted LA-MC-ICP-MS). The laser system facilitates a washout period of typically ~1-1.5 seconds (Müller et al., 2009) **(Figure 1)**. All analyses used a 5 Hz laser pulse rate. The ablated signal was smoothed by including three meters of coiled nylon line with 2.4 mm internal diameter between the laser and the mass spectrometers used **(Supplementary File 1)**. Helium flow rate was held constant at 650 ml/min for both instruments utilized in this study **(Table 2)**. All analyses began with two cleaning pulses followed by 20-30 seconds of background collection depending on the analytical session. Background counts were largely negligible and/or invariable (**Figure 1**; see below) between sessions and so the limit of detection does not drastically change from session to session. Ablation in zircon grains was 30-40 seconds for LA-Q-ICP-MS and 30 seconds for LA-MC-ICP-MS followed by a 10 second washout. For quadrupole analyses the laser was run in energy mode at a constant 5 mJ of energy on a 30 μm spot. For multicollector analyses, energy was controlled with fluence mode at a constant 3.5 J/cm^2 on spot sizes ranging from 16-30μm, with the majority using a 30μm spot (**Supplementary File 1**). Other relevant instrumental parameters are described for both methods utilized in this study immediately below and in **Table 2**.

The discussion of ages below includes external comparison of LA and SIMS U-Pb ages. One notable advantage of SIMS is the shallow depth of the sputtered ion beam crater relative to the crater created by LA. Older U-Pb ages may therefore be more prevalent in the LA dataset due to depth of sampling in the crystals. Estimation of crater depth using a z-calibrated microscope stage resulted in an average of 14 μm deep craters for zircons measured in this study, or ~ 0.09 μm / pulse, similar to prior estimates of 0.06 μm / pulse (Kelly et al., 2014). These crater depths are significantly deeper than the 0.05 μm crater depth created during SIMS analyses (Kern et al., 2016) to which we compare the LA analyses below.

LA-Q-ICP-MS: Tuning was conducted daily on NIST-612 glass immediately prior to the start of each analytical session. Analytes include all relevant isotopes to the U-Pb system (**Table 2**). ThO/Th was limited to ≤1.5% during daily tuning and typical nebulizer flow was optimized between 1-1.1 l/min of Ar. Optimized dwell times are reported in **Table 2** though it should be noted that we report data gathered with multiple dwell times here due to its effect on the reduction methods that we have applied.

LA-MC-ICP-MS: Tuning was done on standard glass GSD-1G. After aligning peaks by adjusting the split-octupole voltages accordingly, gas flow rates, voltages, and the ESA were tuned for sensitivity. Voltages assigned for each collector and the split-octupole were then slightly adjusted again to optimize peak shape. Integration time was set to 0.1 seconds for all isotopes throughout the analyses. The detector array in the NuPlasma 3D multicollector includes Faraday cups, Daly photomultipliers, and ion counters **(Table 3)**. Multiple detector types in the collector block are particularly desirable in U-Pb geochronology (e.g., Kylander-Clark, 2020; Simonetti et al., 2005) as low abundance isotopes can be measured on detectors with relatively low detection limits whereas larger ion beams can be placed on relatively stable Faraday cups. We found that baselines on Faraday cups (equivalent to 5000 – 6000 cps) were insufficient for detection of zircons in the age range of interest here **(Table 3)** that have ^{207}Pb intensities on the order of several hundred to a few thousand counts per second, consistent with prior determinations on the same instrument model (Kylander-Clark, 2020). Daly photomultipliers (≤ 20 cps) and electron multipliers (≤ 1 cps) have baseline counts sufficiently low to measure these relatively small Pb isotope beams. We measured ^{207}Pb measured on the Daly photomultiplier, which shows greater stability and lower drift, though we did observe high backgrounds that increase the baselines to several hundred cps (detail below). The ^{204}Pb signal (10’s to a few hundred counter per second) was measured using the electron multiplier, although we noted greater levels of analytical drift and instability on this detector.

Solution MC-ICP-MS: We also measured the lead isotope composition of feldspar separates to estimate the common Pb isotope composition during zircon crystallization for corrections of common lead in zircon using TW-Concordia. Measurements were made using a NuPlasma3 at OSU with a sample-standard bracketing protocol. A full description of the methodology from mineral separation to data reduction and the values and errors are provided in **Supplementary File 1 and Supplementary File 2,** respectively.

Treatment of LA-Q-ICP-MS Data

Detection limits (DL) for all LA-ICP-MS data gathered in this study (quadrupole and multicollector) were calculated according to Longerich et al. (1996). Mass 202 and 204 were monitored but 204 signal was below DL unless inclusions were intersected. Background subtraction for all LA-ICP-MS data collected in this study was done by selecting an interval after washout of the cleaning pulses and before the start of ablation (~25 seconds; **Figure 1**). Mean intensity of the background was then subtracted from the gross intensity in the selected ablation interval (**Figure 1**) (Longerich et al., 1996).

Elemental fractionation between Pb and U during downhole ablation (Eggins et al., 1998) was accounted for by fitting an exponential curve through the time resolved $^{206}Pb/^{238}U$ (Paton et al., 2010). Error on the ratio was calculated using the standard error at the intercept (Košler et al., 2002). Instrumental mass bias on all isotope ratios was corrected by normalizing to the offset of the primary standard from its accepted age (Košler and Sylvester, 2003).

The Temora-2 standard zircon (Black et al., 2004) was used as a primary standard for all analyses gathered in this study. Secondary standards included various standard zircons supplied to us by the PlasmAge consortium (George Gehrels; Personal Communication), including Fish Canyon Tuff - Schmitz and Bowring, 2001; 94-35 - Klepeis et al., 1998; Plešovice - Sláma et al., 2008; R33 - Black et al., 2004; 91500 - Wiedenbeck et al., 1995; FC-1 - Paces and Miller, 1993; Oracle – Bowring, unpublished; Tan-BrA – Pecha, unpublished; and OG-1 - Stern et al., 2009. Secondary standard ages we obtained for this work are within a few percent of the accepted values and are reported in **Supplementary File 2 and Table 2.**

The low ion yield of the quadrupole mass analyzer (**Table 1**), short dwell times relative to continuous monitoring (0.2 – 0.45 ms), and duty cycle losses associated with sequential analysis means that some analyzed isotopes, notably ^{207}Pb, have low count rates that causes many of the detector passes to have zero counts per second (**Figure 1, Figure 3**). Historically and as per current community accepted practice the ^{207}Pb/^{206}Pb ratios from these analyses would be reduced by taking a mean and a standard deviation (or standard error) (Horstwood et al., 2016). The underlying assumption here is that the data are normally distributed. By definition, the normal distribution has a support from positive to negative infinity; in other words, the normal distribution can take on any value from negative infinity to infinity unless it is explicitly truncated (**Figure 2**). However, a negative ^{207}Pb/^{206}Pb cannot exist in nature and we speculate (based on our experience) that when this issue arises analysts typically truncate the data at zero before calculating a mean, effectively acknowledging 1) that Gaussian treatment of ^{207}Pb/^{206}Pb is invalid and 2) that it is ambiguous as to whether zero counts were generated due to statistical variance for a signal with low average counts per second, or because there were truly no ^{207}Pb ions produced by ablation during that pass. This is likely to introduce an artifact into the data processing and we have explored two methodologies capable of dealing with non-normally distributed ^{207}Pb/^{206}Pb ratios and the two possible sources of zero values. For the remainder of this publication, we refer to the standard reduction of ^{207}Pb/^{206}Pb (i.e., taking a mean and standard error) as the "H16 approach" or simply "H16" after the seminal work of Horstwood et al. (2016).

Zero-Inflated Poisson (ZIP): Digitized values from isotopes with abundances close to zero in LA-Q-ICP-MS analyses are difficult to deal with for two primary reasons: 1) The analyst cannot know *a priori* whether a zero value at any given pass of the detector was due to the true absence of that ion in the sample or if the zero value was generated from random variability in the numerous instrumental and physical parameters operating in the instrument **(Figure 1)**, and, 2) a normal distribution of the counts and consequently their errors extend not only over the LOD but also into zero and negative values **(Figure 2).** Using a Gaussian distribution fundamentally assumes that the value may take on zero or even negative values (Casella and Berger, 2002), although there cannot be negative numbers of isotopes in a real crystal.

ZIP is a distribution that was derived by Lambert (1992) to deal with the possibility that zero values may be generated by both an underlying physical process as well as random variability about a true mean that is close to zero. For the current application the former of these is represented by total loss of ^{207}Pb transmission from ablation site to detector. The possibility that the underlying process has generated the zero value is estimated by a Bernoulli process with probability *p* of a zero occurring. The compliment (1 - p) assigns the distribution to a Poisson log-linear regression process.

Parameters for ZIP were estimated through maximum-likelihood estimation (MLE) by implementation of the Newton-Raphson algorithm. Expected value (E) and variance (V) of the total counts are calculated as:

1) $E[X] = (1 - p)\lambda t$

2) $V[X] = \lambda t(1 - p)(1 + p\lambda t)$

Where p is the probability that the underlying process has generated a zero value, λ is the count rate, and t is the dwell time. It is worth pointing out that the ZIP model is similar to basic Poisson statistics in that the minimum count rate required to see one total count is still dictated by the dwell time.

ZIP cannot be applied directly to the dimensionless $^{207}Pb/^{206}Pb$ as the units are no longer in counts, which is a required assumption for all Poisson processes. Means and standard deviations of the time-resolved ^{206}Pb signal cannot be used as the denominator because this would result in a $^{207}Pb/^{206}Pb$ ratio of counts over counts per second. Even if ^{206}Pb were first converted into counts before taking a mean, this would also lead to a Poisson random variable over a Normally distributed random variable which do not share the same support, making the ratio invalid. ^{206}Pb was therefore reduced using the Poisson distribution, which is effectively normally distributed at count rates observed in this study (i.e., ≥100’s). There is also no successful derivation of a variance for the ratio of two Poisson random variables largely because this would allow for zero values in the denominator. Given these limitations, standard errors from the ZIP and Poisson distribution for ^{207}Pb and

^{206}Pb, respectively, were added in quadrature to the propagated uncertainty of the ages reported here.

Zero-Truncated Normal (ZTN): ZTN is derived directly from the normal distribution. Parameters for ZTN are simply rescaled from the normal based on the chosen truncation points and the ratio of the probability density function to the cumulative distribution function evaluated at rescaled points. This contracts the density between the two truncations, shifting the mean and shrinking the variance. Because of the latter, it is critical to prove that the limiting precision on ^{207}Pb/^{206}Pb in analyses here is smaller than what is predicted by using a Gaussian distribution. Fortunately, this is done by utilizing a Poisson process (Vanhaecke and Degryse, 2012) as described above.

Truncation points for all analyses in this study were set to zero and the maximum ^{207}Pb/^{206}Pb ratio observed in the selected ablation interval (no ablation spikes removed). Mean and variance of the ZTN is:

$$3)\ E[X] = \mu - \sigma\frac{W}{Z}$$

$$4)\ V[X] = \sigma^2\left(1 - \frac{Q}{Z} - \left(\frac{W}{Z}\right)^2\right)$$

For

$$5)\ W = \varphi\left(\frac{b - \mu}{\sigma} - \frac{a - \mu}{\sigma}\right)$$

$$6)\ Z = \phi\left(\frac{b - \mu}{\sigma} - \frac{a - \mu}{\sigma}\right)$$

$$7)\ Q = \frac{b-\mu}{\sigma}\,\varphi\left(\frac{b-\mu}{\sigma}\right) - \frac{a-\mu}{\sigma}\,\varphi\left(\frac{a-\mu}{\sigma}\right)$$

Where a is the lower truncation point, b is the upper truncation point, μ and σ are respectively the mean and standard deviation from the corresponding Gaussian distribution, the function $\varphi(\bullet)$ is the Gaussian probability distribution function as dependent on input parameters in the parentheses above $(\bullet)$, and the function $\phi(\bullet)$ is the Gaussian cumulative distribution function.

<u>Treatment of LA-MC-ICP-MS Data</u>

The significantly higher sensitivity, precision, and the use of different detector types on the U-Pb isotope system provided by LA-MC-ICP-MS analyses requires different methods of data treatment. Measured $^{238}U/^{235}U$ in unknown zircons were corrected for mass bias assuming a $^{238}U/^{235}U$ ratios measured in zircon standard materials of 137.818 (Hiess et al., 2012) and an exponential mass bias model (**Table 2**). $^{207}Pb/^{206}Pb$ and $^{206}Pb/^{204}Pb$ were then reduced by using the standard practice of taking a mean and standard deviation (Horstwood et al., 2016). Mass bias on the $^{207}Pb/^{206}Pb$ ratio was corrected by inclusion of the bias into a bulk fractionation factor (Košler and Sylvester, 2003).

We attempted the curve-fitting approach for the U-Pb downhole correction procedure described above. However, residuals in the regressions of the time resolved Pb/U ratios showed numerous artifacts: funneling, curvature, and non-normality were all present. Whereas the first two could easily be explained by complex elemental fractionation at the ablation site, the last is more precarious. Poor residuals and drastic changes in the ratio were worst near the start of ablation, implying that the time differential was generated by the tau correction on the

Faraday. This observation has also been recorded for single laser pulse experiments using a similar multicollector array (Cottle et al., 2009). Pb/U ratios were therefore reduced by integrating background subtracted signals on each isotope then taking the ratio; the so-called total counts approach (Cottle et al., 2009; Johnston et al., 2009; Pullen et al., 2018). Error on the ratio was calculated according to the standard error on the time-resolved ablation interval selected during data reduction. Mass bias on the Pb/U ratios were dealt with by applying a factor derived from the offset between the $^{206}Pb/^{238}U$ ratio corresponding to the accepted standard age and the measured $^{206}Pb/^{238}U$ ratios, which theoretically accounts for all sources of mass fractionation (i.e., mass fractionation associated with cross-gain calibrations, downhole fractionation at the ablation site, preferential elemental ionization and extraction, and mass dependent sensitivity) (Gehrels et al., 2008; Košler and Sylvester, 2003) as long as this is similar between standards and unknowns.

Significant memory effects on all masses measured on Daly photomultipliers and ion counters were present after tuning. Analysis of the background throughout analytical sessions shows the memory decreased with time after tuning (especially on the ^{204}Pb ion counter) and was not influenced by measurements of zircons with high Pb concentrations (e.g., 91500). We interpret that the memory is derived from contaminant Pb coated onto the torch assembly, sample cone, or lenses from samples and standards measured during prior analytical sessions; a well-documented observation for MC-ICP-MS analyses (Albarède et al., 2004; Collerson et al., 2002). Nevertheless, significant analytical drift was observed and best accounted for by using the sliding window correction (Gehrels et al., 2008). We found normalizing to the nearest six standards was enough to remove any slope in the secondary standard ages and thus this drift correction was applied to the isotope ratios for unknowns. Secondary standard reproducibility and precision are reported in **Table 2**.

Age Reduction

Time-resolved analyses were reduced using the LaserTRAMZ software that was developed in-house and is freely available online (https://github.com/Lewisc2) (Lewis et al., 2023).

Isotopic composition of common Pb used to correct for non-concordant analyses using TW-Concordia was taken from the measurements of feldspar separates described above (**Supplementary File 1, Supplementary File 2**). Errors on the feldspar Pb ratios were propagated into final age reduction. Below we report data as percent concordant based on the deviation between concordant $^{206}Pb/^{238}U$ and $^{207}Pb/^{206}Pb$ ratios using the fraction of common Pb as an estimate. Correction for initial Th disequilibrium (Schärer, 1984) was done assuming a value of 0.33 for $D_{Th/U}$ in zircon (Rubatto and Hermann, 2007). Decay constants found by Jaffey et al. (1971) and Cheng et al. (2000) were used for U and Th decay constants, respectively. Errors on U decay constants include the additional error from counting statistics (Mattinson, 1987). Average uncertainty for primary standard analyses and their respective TIMS errors are included in uncertainty calculations. Reported U-Pb dates for individual zircons are the dates projected through the analyses from common Pb onto TW-Concordia, as reviewed and described by Vermeesch (2018). Uncertainties are reported as 2SE. All pertinent information on data gathered during this study, including dates, are reported in **Table 2** and the **Supplementary Files.**

Results

U-Pb LA-Q-ICP-MS Dates

Puripicar Ignimbrite (PPI): Most U-Pb analyses calculated using the H16 approach from the PPI cluster close to TW-Concordia ($^{207}Pb/^{206}Pb \sim 0.05$-$0.07$; ≥95% concordant), with few analyses having $^{207}Pb/^{206}Pb$ values **(Figure 5A)**. Treating the $^{207}Pb/^{206}Pb$ with the ZIP and ZTN methods results in individual zircon analyses that are more closely grouped, but also slightly further away from TW-Concordia ($^{207}Pb/^{206}Pb \sim 0.07$-$0.10$; 91-89% concordant). Following from above, this heuristically makes sense in the ZTN case as the entire Gaussian distribution is compressed between two points, resulting in more right skewness in calculated $^{207}Pb/^{206}Pb$ ratios. In the ZIP case, this is either caused by underestimation of zero values associated with random variability in the Poisson component of the distribution (see equation 1), or the data are affected by the dwell times in some manner (30ms and 20ms for ^{207}Pb and ^{206}Pb, respectively). U-Pb analyses with greater amounts of common Pb also have distinctly larger errors under the ZIP treatment. Using ZTN causes the analyses to become more dispersed but closer to Concordia than the ZIP treatment.

Mean fully propagated errors on the $^{206}Pb/^{238}U$ age for PPI zircons using the H16 approach is 25.3%. Errors are smaller when using the ZIP (18.7%) and ZTN (16.1%) treatment.

Zircon U-Pb dates reduced using various methods in the PPI are almost ubiquitously within error of one another despite differences in concordance **(Figure 5B)**. The youngest seven dates are shifted towards younger dates when ZTN is used, with one age being shifted more than 50%. These are the dates with a greater common Pb component, which are significantly more dispersed under the ZTN treatment **(Figure 5A)**.

Middle Block and Ash Flow (MBA): U-Pb LA-Q-ICP-MS dates in MBA were collected using the same dwell times as the PPI **(Figure 5A, Figure 5C)**. Distribution of $^{207}Pb/^{206}Pb$ ratios in MBA zircon analyses near TW-Concordia are broadly within error of one another in a cluster between 0.06-0.15 using the H16 approach (**Figure 5A;** 98-87% concordant). $^{207}Pb/^{206}Pb$ ratios reduced using ZIP are clustered closer together compared to H16 at values between ~0.07-0.15 (96-87% concordant). Like the PPI, zircon analyses fall further from TW-Concordia under both ZIP and ZTN relative to H16.

Mean errors on dates in MBA using H16 are 32.6% **(Figure 5D)**. This is larger than the mean errors using ZIP (29.1%) or ZTN (21.8%). It is also critical to note that of the eruptions discussed here, zircon U-Pb dates for MBA have the largest associated uncertainties.

MBA U-Pb dates measured by LA-Q-ICP-MS are underdispersed between ~2-3 Ma for all treatments here (MSWD ≤ 1.0). Distribution of the dates under H16 is broader than those generated by the ZTN approach or the ZIP approach **(Figure 5D)**. The wider distribution is largely an artifact of the analyses lying closer to TW-Concordia under the H16 approach, as small differences in the isotope ratios has more control on the projected concordant date.

Embaucador Rhyolite (ER): Zircon U-Pb ages from the ER were gathered using two sets of dwell times on ^{207}Pb and ^{206}Pb. The first set was equivalent to the PPI and MBA. The second set was gathered with higher dwell times on both ^{207}Pb (45 ms) and ^{206}Pb (43 ms). $^{207}Pb/^{206}Pb$ ratios for the former are similar to PPI and MBA in that the data reduced using ZIP are slightly more discordant than the corresponding H16 reduction. ^{207}Pb/^{206}Pb ratios in ER zircon analyses gathered with higher dwell times and reduced using the ZIP approach are within error **(Figure 5E)**. Analyses lying closest to TW-Concordia have virtually the same concordance for the H16 approach (94.5%) as they do for the ZIP (94.1%). Zircon grains in ER have the highest fraction of common Pb from all eruptions associated with Cerro Chaxas, with nearly half of the grains measured by LA-Q-ICP-MS having detectable ^{204}Pb. Individual analyses of high common Pb zircons have approximately normally distributed ^{207}Pb intensities, contrasting the other analyses that feature a prominent number of zero values. Calculating a ^{207}Pb/^{206}Pb with the ZIP approach makes these data more discordant than the corresponding H16 reduced data **(Figure 5E)**. Reducing the analyses with the ZTN approach scatters the data more than either the H16 or ZIP approaches though the resulting ^{207}Pb/^{206}Pb ratios are within error.

Mean error on all ER zircon U-Pb dates using H16 is 18.7%, which is slightly lower than the mean error produced from the ZIP method (18.8%). ZTN produces a mean error smaller than either H16 or the ZIP method (14.7%). For the data collected with higher dwell times errors on the ages reduced using the ZIP reduction average 14.1% whereas the errors on the H16 approach average 14.9%.

ER U-Pb dates are strongly overdispersed **(Figure 5F)**. Data collected with lower dwell times and reduced using the ZIP approach form a distinctly young tail owing to the higher discordance that affects the location on the projected concordant age. All data collected with higher dwell times and reduced using the ZIP approach are within error of the corresponding H16 reduced data. ZTN reduced data are broadly similar.

U-Pb LA-MC-ICP-MS Dates

LA-MC-ICP-MS dates (**Supplementary File 1**) are presented in this section for the three zircon aliquots taken from the same samples described above. For simplicity LA-MC-ICP-MS and LA-Q-ICP-MS dates are referred to as MC and Q dates, respectively. Emphasis is placed on the PPI as this eruption was also dated via SIMS by Kern et al. (2016) and is used for discussion of user bias in spot selection below.

Puripicar Ignimbrite (PPI): MC isotope ratios from zircon spot analyses are notably more concordant than Q isotope ratios and have lower $^{238}U/^{206}Pb$ ratios (**Figure 6A**). Discordant data cluster together on the same poorly defined linear array towards common Pb with the exception of some analyses that generated lower $^{238}U/^{206}Pb$ ratios and MC analyses with high $^{207}Pb/^{206}Pb$ ratios.

MC dates are within error of the range of Q dates, though the MC dates are offset to slightly older ages (**Figure 6**) corresponding with their lower $^{238}U/^{206}Pb$ ratios. The five youngest MC dates are distinctly offset by ~0.3-0.8 Ma from the rest of the MC age spectra and are within error of the youngest ages in the Q dataset. Age spectra of both datasets are multimodal with the MC dates forming two satellite peaks at ~ 7.25 Ma and ~ 8.9 Ma whereas the Q dates define only one broad satellite peak at ~ 8.3 Ma.

Middle Block and Ash Flow (MBA): MC dates in MBA are underdispersed (MSWD: 0.7) and well within the range of the similarly underdispersed Q dates (MSWD: 0.16). The only exception to this is a single MC date at 4.8 Ma that was identified as a PPI age antecryst from the Chaxas complex (Lewis et al., 2025). Combining the two datasets forms an age spectrum that overlaps entirely with the exception mentioned above (**Figure 5D**).

Embaucador Rhyolite (ER): MC dates in ER are extremely overdispersed, as are Q dates. MC dates have a thinner upper tail compared to Q dates, producing an overall tighter distribution **(Figure 5F)**. An abundance of young dates in the MC dataset form a distinct perturbation in the age spectra. This is also seen in the H16 and ZIP reduced age spectra but appears washed out in the ZTN reduced Q age spectra.

Comparison of SIMS and LA-ICP-MS U-Pb Dates

SIMS U-Pb dates in the PPI collected by Kern et al. (2016) were gathered from zircons separated from the same pumice samples from the same outcrop as those used to determine the LA-Q-ICP-MS and LA-MC-ICP-MS dates reported here. LA-Q-ICP-MS isotope ratios reduced using ZIP largely overlie the SIMS isotope ratios with the bulk of the SIMS data being more concordant **(Figure 6A)**. $^{238}U/^{206}Pb$ ratios are generally slightly higher in the SIMS dataset compared to LA-Q-ICP-MS data, though all LA-Q-ICP-MS isotope ratios are enveloped by the range of isotope ratios found via SIMS **(Figure 6A)**. Most LA-MC-ICP-MS zircon analyses lie closer to TW-Concordia than either of the other two datasets and have smaller errors on the $^{207}Pb/^{206}Pb$ ratio, owing to simultaneous collection of the two isotopes on Daly photomultipliers. $^{238}U/^{206}Pb$ ratios are generally lower in LA-MC-ICP-MS data than either of the other two datasets, though it should be noted there is a group of analyses with low $^{238}U/^{206}Pb$ ratios in all three datasets.

SIMS U-Pb dates are remarkably less dispersed than LA-Q-ICP-MS dates **(Figure 6B)**. Nevertheless, dates in the lower tails of both datasets overlap within error and form age spectra with broadly the same age range. In the upper tail, distinct groups of LA-Q-ICP-MS dates fall away from the main array of the age spectra. One SIMS analysis and a group of analyses in the LA-Q-ICP-MS that are within error of each other are strongly offset to older ages relative to the rest of the age spectra. LA-MC-ICP-MS dates are generally older than either of the other two datasets. Despite the offset, the youngest group of zircon spot analyses in the lower tail of the LA-MC-ICP-MS distribution are within error of the youngest dates in the SIMS and LA-Q-ICP-MS datasets **(Figure 6B)**. The slope of the largest group of data (**Figure 6B**) is essentially as steep as those in the SIMS dataset. In all three datasets there are dates offset from the main age spectra from 6 Ma – 9 Ma. These satellite peaks are more abundant in LA-MC-ICP-MS dates than either of the other two datasets.

No xenocrysts were found by Kern et al. (2016) in the PPI. Seven xenocrysts with dates ranging from 2 Ga – 25 Ma were found in the PPI during collection of LA-Q-ICP-MS dates in this study **(Figure 7),** despite fewer total analyses. One xenocryst with a date of 432 Ma, similar to LA-Q-ICP-MS xenocryst dates, was found in the LA-MC-ICP-MS dataset.

Discussion

Improved Treatment of the ^{207}Pb/^{206}Pb Ratio in LA-ICP-Q-MS Analyses in Young Zircons

Utilizing distributions that appropriately treat the ^{207}Pb/^{206}Pb ratios as being bound at zero (**Figure 2**) greatly improve precision on measured ^{207}Pb/^{206}Pb ratios and on the final zircon U-Pb ages (**Figure 5, Table 4**). One undesired outcome, however, is that in some cases, use of these distributions may raise the ^{207}Pb/^{206}Pb ratios and generate more discordant data (**Table 4**). Compression of the normal distribution using ZTN shrinks the overall range of values for the $^{207}Pb/^{206}Pb$ ratio and reduces uncertainty. However, the same compression that reduces the error also fattens the tail, generating right skew that increases the $^{207}Pb/^{206}Pb$ ratio. The net impact of this is to cause more discordance compared to the H16 approach **(Figure 5A, 5C, 5E; Table 4).** Change in concordance when using ZIP is discussed further in the following section as there is a clear artifact in concordance generated by dwell time dependence that warrants further explanation.

Applying distributions with the appropriate support for zero values also reduces age uncertainties, with $^{206}Pb/^{238}U$ ages for individual analyses reduced on average by 1 – 7 % (absolute) using the ZIP and ZTN methods compared to H16 (**Table 4**). For zircons in this study with ages between 1 Ma – 10 Ma, the uncertainty on an individual analysis was reduced by up to 400 k.a., which is a significant improvement. Although both ZTN and ZIP approaches produced reduced uncertainties, we recommend the ZIP due to the differences in concordance (**Table 4**).

Improved precision in U-Pb geochronology is highly desirable not only for reducing the uncertainty on ages but also when considering treatment of datasets. Analysis of variation in ages with respect to the analytical uncertainties (e.g., Vermeesch, 2021) and parameterized zircon crystallization models that attempt to resolve the discrete magmatic events that contribute to otherwise densely spaced U-Pb age spectra (e.g., Tavazzani et al., 2023) rely heavily on the errors associated with each analysis. Therefore even small improvement of error on U-Pb dates can change the interpretation on the number of events suggested by zircon ages populations.

Effect of Dwell Times

We also observed some variations in our data related to changes in dwell times for individual mass peaks. Reducing the $^{207}Pb/^{206}Pb$ ratio using a counts-based approach on the two contributing isotopes would ideally be unaffected by dwell time other than to improve counting statistics and the final precision on the ratio. If this were true, changing dwell times would cause no observable systematic variation. However, we observed that U-Pb data collected with dwell times of 30ms and 20ms on ^{207}Pb and ^{206}Pb, respectively, were systematically displaced from TW-Concordia towards higher $^{207}Pb/^{206}Pb$ ratios relative to data collected with higher dwell times (**Table 4**).

Zircons from datasets collected with dwell times of 30 ms on ^{207}Pb and 20 ms on ^{206}Pb demonstrate the discordance artifact well. $^{207}Pb/^{206}Pb$ ratios in PPI and MBA zircons are offset further from Concordia when using ZIP compared to H16 (**Figure 5A, 5E**). PPI $^{207}Pb/^{206}Pb$ ratios change from ~0.05 to ~0.1 from H16 to ZIP, equating to a roughly 5% difference in concordance. The offset towards common Pb is exacerbated in analyses with higher (≥ 0.1) $^{207}Pb/^{206}Pb$ ratios **(Figure 5A)**. A similar relationship is observed in MBA (**Figure 5E**) and for those ER zircon U-Pb analyses collected with low dwell times. $^{207}Pb/^{206}Pb$ ratios in ER zircons collected using higher dwell times and reduced using the ZIP approach are similarly concordant to those $^{207}Pb/^{206}Pb$ ratios reduced by H16 **(Figure 5C; Table 4)**.

Systematic offset of the $^{207}Pb/^{206}Pb$ ratios in zircons collected with lower dwell times is reconciled when considering the effect that the dwell time has on the observed counts and the expected value of the ZIP model (equation 1). Increasing the dwell times reduces the count rate required to see a single count (e.g., 40 cps for a 25 ms dwell time), causing an effective increase in sensitivity at low count rates due to more continuous monitoring. Assuming that the two sources of zero values are non-existence of a ^{207}Pb atom in an analyzed volume and no transmission of an existent ion, observing higher total counts should increase the probability that an observed zero value is generated from the latter (underlying) process, as the higher total counts give more certainty that the relevant atoms are indeed present. In turn, this causes the expected value of the ^{207}Pb counts to decrease under the ZIP model despite observing higher count rates (equation 1). The estimated parameter p in equation 1 for the datasets confirms that this is the case. Values for this parameter are highest for the nearly concordant data collected with higher dwell times (**Figure 8**). More discordant data also have a higher value for this parameter when collected with higher dwell times though the relationship is not as prominent.

Biases in Spot Selection of *in-situ* U-Pb Methods

Significant differences between the age spectra and proportion of xenocrysts generated from all three methods used to gather zircon U-Pb ages for the PPI suggests non-analytical bias exists between them (**Figure 6B; Figure 7**). LA-ICP-MS data show that the Puripicar ignimbrite hosts significantly more xenocrysts than previously documented (**Figure 7**). In fact, the xenocrysts in the Puripicar ignimbrite span the age range of Proterozoic to Cambrian ages recorded in lower crustal xenoliths in the South American Andean arc (McLeod et al., 2013) (~0.5 Ga – 2 Ga) to Ordovician to Neogene ages (~480 Ma – 20 Ma) corresponding to upper crustal lithologies in the area surrounding the Chaxas Complex (Lucassen et al., 2001). Prominent satellite peaks in the LA-ICP-MS datasets also reveal a higher proportion of antecrysts in the juvenile clasts of the Puripicar ignimbrite than what would be inferred from the nearly unimodal SIMS dataset (**Figure 6B**). Two distinctly different interpretations regarding recycling of stored near- to sub-solidus magmatic material and assimilation within the PPI magmatic system would be drawn from the SIMS and LA data. While details on these interpretations are outside the context of the current work, we address possible sources of non-analytical bias between the datasets.

Offset Puripicar LA-MC-ICP-MS Age Spectra: As pointed out above, the youngest U-Pb ages for all three datasets overlap at the 2s level (**Figure 6B**). However, PPI dates gathered by LA-MC-ICP-MS are characteristically older than those in the other two datasets. One explanation for this offset is that the fractionation correction on the $^{238}U/^{206}Pb$ ratio using the much older standards is not accurately capturing the cross-gain differences between Faraday cup and Daly photomultiplier detectors in MC analyses. However, dates for MBA are underdispersed within combined Q and MC datasets (Supplementary File 1) suggesting that there is not systematic offset associated with analytical issues (i.e., gain calibrations) between MC and Q measurements. While it could be argued that gains were drifting throughout the analytical sessions, it would be overwhelmingly serendipitous for the gain ratios to drift appropriately for the MBA LA-MC-ICP-MS U-Pb dates to completely overlap with all LA-Q-ICP-MS data but no other sample (note ER U-Pb dates overlap as well; **Figure 5D**).

One alternate scenario is these differences instead reflect contribution of larger grain size zircons and/or preferential spot selection during LA-MC-ICP-MS analyses. Although the proportion of core and interior analyses are higher in the LA-MC-ICP-MS dataset, spot selection does not explain the offset because the zircon grains are generally homogenous with respect to age (**Supplementary File 1**). However, zircon crystals selected for LA-MC-ICP-MS analyses were larger overall than the other two methods (**Figure 6C**), and this is taken as the most likely explanation for the offset, in conjunction with fewer total analyses in the LA-MC-ICP-MS dataset.

Bias between SIMS and LA-Q-ICP-MS data sets: Differences in grain size are less tenable as the explanation for the differences between SIMS and LA-Q-ICP-MS data, due to the similarities of grain size between the two sets of zircons of analyzed (**Figure 6C**). However, this still leaves the possibility of bias in selection of analytical locations between the two studies. Only one spot per grain was measured during SIMS analyses (**Supplementary File 1**) and as a result, complexly textured zircon grains with bright cores appear to be generally avoided as analysis targets (**Table 5**). This occurs in many studies as it is well-documented that these domains are frequently characterized by crystal defects and trace element substitution that compromises the U-Pb isotope system (Pidgeon, 1992; Vavra, 1990; Vavra et al., 1999), including Pb loss due to recrystallization during fluid-present recrystallization or high temperature metamorphism (Grant et al., 2009; Vavra et al., 1999). In this regard, avoiding these zones was understandable given the regional scope and goals of the study conducted by Kern et al. (2016). Nevertheless, we point out that critical interpretations, regarding the thermal regime and long-term construction of the magmatic system based on age spectra should have accounted for this preference.

In addition to targeted spot selection, differences in measurement volume between LA and SIMS may also generate significant bias. Although spot sizes are comparable (SIMS: 25-30 μm; LA: 30 μm), the 0.5 μm crater depth of SIMS analyses for the PPI zircons are ~4% of the depth of LA craters. This could introduce a bias for older ages in the LA analyses due to intersection of multiple growth zones and indeed downhole changes in $^{206}Pb/^{238}U$ and $^{207}Pb/^{206}Pb$ ratios were observed (and avoided) in some LA analyses. Both studies, however, also utilized sectioned zircon grains that had exposed cores and complexly textured grains indicative of multiple growth events. Given the physical exposure of full crystal growth history in both studies sampling volume cannot be a major consequence of bias between the two datasets. Even if it were, this does not change the fact that there is a missing age component in the original SIMS study exhibited by numerous xenocrysts in the LA study.

In order to assess if there is an inadvertent bias in interpretation of U-Pb age data based on spot selection guided by CL-texture in the study of Kern et al. (2016) a weighted mean of both datasets was first taken (excluding xenocrysts with ages ≥ 10Ma). U-Pb ages younger than the weighted mean at the 1s level (mean – 1s) were classified as “young”. U-Pb ages greater than the weighted mean were classified as “old” (mean + 1s). All others were considered “average”. CL-textures for spot locations were classified as bright, grey, and dark (**Supplementary File 1**). Crude odds ratios (Ramsey and Schafer, 2013) were then used to initially assess if there is a bias in the chances of seeing an “old” age as well as a spot selection in a “bright” core. Results of this simple calculation indicate that the two datasets are offset from unity in opposite directions (**Table 5**) implicating a bias.

Quantitative bias analysis is a method frequently used by epidemiologists to address participation or selection bias in studies (Lash et al., 2009). Equations and more detailed explanations are given in **Supplementary File 1**, but for the purpose of our application quantitative bias is explained heuristically. The simplest way to conceptualize quantitative bias is to ask a simple question such as: “Out of all the mail surveys and in-person solicitations I’ve had to answer about some topic, what is the proportion of times I said yes, and did I have a personal interest in the topic when I did agree to take the survey?”. Given the clear participation bias related to interest, it is then necessary for epidemiologists to resample the population of interest a second time (characterized non-participants) to deal with the participation bias. Usually, no information is gathered on the initial, uncharacterized proportion in the initial sampling. In the case of spot selection during zircon U-Pb dating, however, characteristics of the non-participants are in fact captured in the CL-texture in unanalyzed spots in the crystals (**Figure 8**).

Using the CL-texture and age classifications described above, spot analyses were classified for the SIMS dataset and are considered the initial participants in the study. Spot analysis collected by LA-Q-ICP-MS were then classified as above and are considered to be characterized non-participants as these are in effect a resampling of the initial sampled population in the SIMS study. Unmeasured cores and rims were then classified from CL-images of the SIMS grains and are appropriately considered non-participants of the initial study, which may be elucidated by the characterized non-participants. A conceptual diagram of this application is shown in **Figure 9** along with an example table of counts, odds ratios, and adjusted odds ratios. Odds of seeing an “old” and “bright” CL-textured core are strongly biased in opposite directions of unity between the two datasets (**Table 6**). The affinity for seeing “old” and “bright” CL-textured cores in the LA-Q-ICP-MS dataset is so large that adjusting the odds in the SIMS dataset changes the association from zero to

1.80, indicating that it is extremely likely that the important, older age component was missed during the SIMS study due to targeted spot selection.

Some bright cores were measured in the SIMS study, addressing the question of why no xenocrystic zircon domains were found if this is the texture that these age domains typically display. Analysis of the SIMS grains shows those cores were selected in generally homogenously textured grains and only one spot per grain was chosen (**Supplementary File 1**). Multiple spots per grain were chosen for the LA-Q-ICP-MS datasets regardless of texture. Compared together, these datasets suggest that characterization of zircon grains should be completed to the greatest extent possible (i.e., quality CL-images, and more than one spot per grain) if the goal or interpretations of the study will include thermal histories across time. Whereas the Kern et al (2016) study is valid for characterizing the pre-eruptive magmatic evolution of the upper crustal APVC silicic magma systems, the objectives of that study did not produce a data set that adequately addressed the earlier history of the magmatic system.

Spatial texture and age analysis presented here through quantitative bias reinforces the importance of considering textural types in the selection of spots during analysis, although it is very rare that a quantitative or randomized approach is taken to such sample selection. In this context, the relative affordability and convenience of the LA-ICP-MS approaches (both Q and MC) facilitates a more comprehensive survey that has the potential to reveal a more complete inventory of the zircon record and evolution of the magmatic system.

Conclusions and Recommendations

Two data reduction techniques were used on young zircons to address the fundamental observation that reducing $^{207}Pb/^{206}Pb$ ratios in zircon measured by low yield non-magnetic sector LA-Q-ICP-MS should be bound at zero (i.e., no ‘negative’ ion abundance). The first is a counting statistics approach that employs the Zero-Inflated Poisson (ZIP) distribution. Errors on U-Pb dates may be reduced up to a few percent under the appropriate analytical conditions. The Zero-Truncated Normal (ZTN) distribution, also bound at zero, was used to reduce the same data. Errors using ZTN are smaller than those produced by ZIP but analyses were also less concordant due to compression of the normal distribution and the concomitant right skewedness introduced. We recommend that ZTN should be avoided for these types of analyses, especially when considering that most data reduction software trims extreme values that bound the possible range of data to begin with. We suggest application of the ZIP approach for the specific scenario of measuring young (≤ 10 Ma) zircons when using a mass spectrometer with relatively low ion yield (such as a quadrupole) due to the improvement of error and similar concordance to data reduction strategies that assume all isotope ratios are normally distributed during analysis.

U-Pb geochronology was conducted on duplicate zircon splits from the same pumice samples using the much more precise LA-MC-ICP-MS method. Comparison of U-Pb dates shows that the LA-Q-ICP-MS dates agree with LA-MC-ICP-MS dates. A separate study that previously utilized SIMS to gather U-Pb dates from the same ignimbrite outcrops produced an age spectra that also produced similar ages for younger zircons related to the host sample, but also shows significantly fewer grains interpreted as xenocrysts or antecrysts. Quantitative bias models are used to describe how spot selection guided with cathodoluminescence (CL) images results in bias between LA and SIMS datasets. Accounting for this bias shows interpretations on the thermal history and architecture of the system based on zircon age spectra can be strongly dependent on sample selection criteria and impacted by selection biases, although these are rarely quantified. We further suggest that interpretation of U-Pb zircon data should explicitly account for any conscious bias in targeted spot analyses or unconscious bias while making interpretations, and ideally sample selection approaches should employ strategies to avoid such bias, such as randomization. Furthermore, individual grains should be characterized as much as possible when gathering in-situ U-Pb dates (i.e., quality CL-images and more than one spot per grain if possible).

Figure Captions

Figure 1) Time-resolved analysis of U-Pb data in zircon showing raw intensities of select isotopes used to calculate U-Pb dates. Intensities of ^{207}Pb are frequently observed at zero throughout the duration of the ablation but are above the limit of detection. Annotations show cleaning pulses, background, ablation interval, and washout.

Figure 2) Normal probability distributions of ^{207}Pb intensities from U-Pb LA-Q-ICP-MS analyses analyzed during a single analytical session. Distributions are distributed between the 1st and 99th percentiles. Red region on left side shows region of negative values that are within the bounds of the normal distribution but violate the fact that a negative number of ^{207}Pb atoms cannot be in a zircon grain.

Figure 3) Time-resolved ablation interval from two zircon analyses in the Embaucador rhyolite showing $^{207}Pb/^{206}Pb$ ratios. A) Zircon grain with no zero values in ^{207}Pb intensity. Vertical histogram of ratio on right is approximately normally distributed, satisfying H16 assumptions. B) Typical zircon grain with isotopic ratios placing the analysis close to TW-Concordia. Vertical histogram shows abundant zero values in the $^{207}Pb/^{206}Pb$ ratio stemming from no detected ^{207}Pb. Distribution of the ratio is not approximately normal.

Figure 4) Generalized geologic map of Cerro Chaxas and associated eruptions generalized into lithologic groups or formations. Chilean-Bolivian border shown in thick white line with respective country names on appropriate side of border. Thin black lines show 300m contour intervals. Pink text shows active arc volcanoes. Inset diagram shows the spatial distribution of the APVC and Chilean-Argentinean-Bolivian borders.

Figure 5) Tera-Wasserburg Concordia (left column) and zircon U-Pb age spectra (right column) for the Puripicar Ignimbrite (PPI, top row), Embaucador Rhyolite (ER, middle row), and Middle Block and Ash Flow (MBA, bottom row) of the Chaxas Complex. Vertical histograms on Concordia show distribution of $^{207}Pb/^{206}Pb$ ratios for each reduction type colored the same as the data points. Dwell times (Dt) used during each analytical session shown. PPI and MBA have distributions of $^{207}Pb/^{206}Pb$ ratios reduced using ZIP that are offset towards common Pb relative to the H16 approach. ER data collected with high dwell times does not show this but rather shows more tightly distributed data near Concordia. $^{207}Pb/^{206}Pb$ ratios reduced using ZTN tend to be offset towards common Pb relative to the H16 approach. ER data collected with low dwell times are shown as partially transparent and are not used in the histogram of $^{207}Pb/^{206}Pb$ ratios.

Kernel density estimates (KDEs) are shown for each reduction type on U-Pb age spectra with colors that match data points. Black lines on age spectra show LA-MC-ICP-MS U-Pb KDEs, which largely overlap with LA-Q-ICP-MS KDEs. Mean fully propagated (2s) errors from all analyses shown using the various approaches are shown on U-Pb age spectra. Errors are substantially smaller for ZIP and ZTN compared to H16.

Figure 6) A) Tera-Wasserburg Concordia showing SIMS, LA-Q-ICP-MS, and LA-MC-ICP-MS analyses from the PPI. Horizontal and vertical histograms respectively show distribution of $^{238}U/^{206}Pb$ and $^{207}Pb/^{206}Pb$ ratios colored the same as the data points. Note the offset of LA-MC-ICP-MS and LA-Q-ICP-MS ages cannot be accounted for by gain calibrations or analytical differences (see text). LA-Q-ICP-MS dates largely overlap with SIMS ages. B) U-Pb age spectra from data collected from each methodology used or discussed here. LA-ICP-MS methods are significantly more dispersed than the SIMS data, the latter of which lacks xenocrysts (Figure 7) that are prevalent in LA data. C) Box and whisker plots of sectioned zircon length and width.

Figure 7) Xenocryst ages collected by LA-ICP-MS. Highlighted fields in background show the range of zircon ages found in lower crustal xenoliths by McLeod et al. (2013) defining the Paleoproterozoic, Mesoproterozoic, and Phanerozoic peaks. Black box shows Puripicar ignimbrite xenocrysts. Other data points are xenocrysts from eruptions associated with the Chaxas complex.

Figure 8) Concordance (expressed as percent) versus the modeled zero-inflation constant for the ZIP distribution (equation 1). Data collected with higher dwell times have a higher constant.

Figure 9) Explanation of quantitative bias analysis as applied to CL-images and U-Pb dates in zircon. A) Two CL-images of zircon grains measured by LA-Q-ICP-MS. Grains are internally complex with numerous truncations and overgrowths. B, C) Traced representations of CL-images measured by LA-Q-ICP-MS and SIMS. Red dots and annotations show actual spots and dates. Blue, pink, and gold dots and annotations show hypothetical spot selections and dates used to show how a bias may be present. Pink dots are initial studied 'samples' (i.e., the participants). Blue dots are a characterized re-sampling of the same population, in this case zircons collected from pumice of the same outcrop as the initially sampled population (i.e., the characterized non-participants). Gold dots show portion of population that was left uncharacterized (Non-participants). Assessing the relationship between spot location (core vs rim) and date of that spot for the initial participants population and characterized non-participants population are offset strongly in opposite directions of unity, implicating a bias is present (see Table 5). Adjusting the odds of the hypothetical data using the minute information known about the non-participants (the location) amongst the other data shows the odds go back to the other side of unity when non-participants are accounted for. See Supplementary File 1 for equations and traced CL-images.

Acknowledgements

We have extensive gratitude for the VIPER group at OSU who provided thorough critique and comments on this manuscript, with particular thanks to Anita Grunder and John Dilles. Samples from various outcrops at Cerro Chaxas would not have been attainable without the expertise of Christian Metzke and Matias Villarroel. This work was funded through generous research grants awarded to CTL, who is deeply obliged for: GSA Lipman Student Research Grant, Mazamas Graduate Research Grant, a Central Oregon Geoscience Society Student Grant, the Jack Kleinman Memorial Fund, and the Sharp Family Fellowship at OSU.

References

Albarède, F., Telouk, P., Blichert-Toft, J., Boyet, M., Agranier, A., Nelson, B., 2004. Precise and accurate isotopic measurements using multiple-collector ICPMS. Geochimica et Cosmochimica Acta 68, 2725–2744. https://doi.org/10.1016/j.gca.2003.11.024

Black, L.P., Kamo, S.L., Allen, C.M., Davis, D.W., Aleinikoff, J.N., Valley, J.W., Mundil, R., Campbell, I.H., Korsch, R.J., Williams, I.S., Foudoulis, C., 2004. Improved 206Pb/238U microprobe geochronology by the monitoring of a trace-element-related matrix effect; SHRIMP, ID–TIMS, ELA–ICP–MS and oxygen isotope documentation for a series of zircon standards. Chemical Geology 205, 115–140. https://doi.org/10.1016/j.chemgeo.2004.01.003

Burns, D.H., de Silva, S.L., Tepley, F., Schmitt, A.K., Loewen, M.W., 2015. Recording the transition from flare-up to steady-state arc magmatism at the Purico-Chascon volcanic complex, northern Chile. Earth and Planetary Science Letters 422, 75–86. https://doi.org/10.1016/j.epsl.2015.04.002

Casella, G., Berger, R.L., 2002. Statistical inference, 2nd ed. ed. Thomson Learning, Australia ; Pacific Grove, CA.

Cheng, H., Edwards, R.L., Hoff, J., Gallup, C.D., Richards, D.A., Asmerom, Y., 2000. The half-lives of uranium-234 and thorium-230. Chemical Geology 169, 17–33. https://doi.org/10.1016/S0009-2541(99)00157-6

Collerson, K.D., Kamber, B.S., Schoenberg, R., 2002. Applications of accurate, high-precision Pb isotope ratio measurement by multi-collector ICP-MS. Chemical Geology 188, 65–83. https://doi.org/10.1016/S0009-2541(02)00059-1

Cottle, J.M., Horstwood, M.S.A., Parrish, R.R., 2009. A new approach to single shot laser ablation analysis and its application to in situ Pb/U geochronology. J. Anal. At. Spectrom. 24, 1355. https://doi.org/10.1039/b821899d

de Silva, S., Zandt, G., Trumbull, R., Viramonte, J.G., Salas, G., Jiménez, N., 2006. Large ignimbrite eruptions and volcano-tectonic depressions in the Central Andes: A thermomechanical perspective. Geological Society Special Publication 269, 47–63. https://doi.org/10.1144/GSL.SP.2006.269.01.04

de Silva, S.L., 1991. Style of zoning in central Andean ignimbrites; Insights into magma chamber processes. Geological Society Special Publication 217–232.

de Silva, S.L., 1989. Altiplano-Puna volcanic complex of the central Andes. Geology 17, 1102–1106. https://doi.org/10.1130/0091-7613(1989)017<1102:APVCOT>2.3.CO;2

de Silva, S.L., Francis, P.W., 1989. Correlation of large ignimbrites - Two case studies from the Central Andes of northern Chile. Journal of Volcanology and Geothermal Research 37, 133–149.

Dröllner, M., Barham, M., Kirkland, C.L., Ware, B., 2021. Every zircon deserves a date: selection bias in detrital geochronology. Geol. Mag. 158, 1135–1142. https://doi.org/10.1017/S0016756821000145

Eggins, S.M., Kinsley, L.P.J., Shelley, J.M.G., 1998. Deposition and element fractionation processes during atmospheric pressure laser sampling for analysis by ICP-MS. Applied Surface Science 127–129, 278–286. https://doi.org/10.1016/S0169-4332(97)00643-0

Ehrenberg, R.G., Mavros, P.G., 1995. Do Doctoral Students’ Financial Support Patterns Affect Their Times-To-Degree and Completion Probabilities? The Journal of Human Resources 30, 581. https://doi.org/10.2307/146036

Frei, D., Gerdes, A., 2009. Precise and accurate in situ U–Pb dating of zircon with high sample throughput by automated LA-SF-ICP-MS. Chemical Geology 261, 261–270. https://doi.org/10.1016/j.chemgeo.2008.07.025

Gaynor, S.P., Ruiz, M., Schaltegger, U., 2022. The importance of high precision in the evaluation of U-Pb zircon age spectra. Chemical Geology 603, 120913. https://doi.org/10.1016/j.chemgeo.2022.120913

Gehrels, G.E., Valencia, V.A., Ruiz, J., 2008. Enhanced precision, accuracy, efficiency, and spatial resolution of U-Pb ages by laser ablation-multicollector-inductively coupled plasma-mass spectrometry: TECHNICAL BRIEF. Geochem. Geophys. Geosyst. 9, n/a-n/a. https://doi.org/10.1029/2007GC001805

Grant, M.L., Wilde, S.A., Wu, F., Yang, J., 2009. The application of zircon cathodoluminescence imaging, Th–U–Pb chemistry and U–Pb ages in interpreting discrete magmatic and high-grade metamorphic events in the North China Craton at the Archean/Proterozoic boundary. Chemical Geology 261, 155–171. https://doi.org/10.1016/j.chemgeo.2008.11.002

Hiess, J., Condon, D.J., McLean, N., Noble, S.R., 2012. 238U/235U Systematics in Terrestrial Uranium-Bearing Minerals 335.

Hildreth, W., Moorbath, S., 1988. Crustal contributions to arc magmatism in the Andes of Central Chile. Contributions to Mineralogy and Petrology 98, 455–489. https://doi.org/10.1007/BF00372365

Horstwood, M.S.A., Košler, J., Gehrels, G., Jackson, S.E., McLean, N.M., Paton, C., Pearson, N.J., Sircombe, K., Sylvester, P., Vermeesch, P., Bowring, J.F., Condon, D.J., Schoene, B., 2016. Community-Derived Standards for LA - ICP - MS U-(Th-)Pb Geochronology – Uncertainty Propagation, Age Interpretation and Data Reporting. Geostand Geoanal Res 40, 311–332. https://doi.org/10.1111/j.1751-908X.2016.00379.x

Jackson, S.E., Pearson, N.J., Griffin, W.L., Belousova, E.A., 2004. The application of laser ablation-inductively coupled plasma-mass spectrometry to in situ U–Pb zircon geochronology. Chemical Geology 211, 47–69. https://doi.org/10.1016/j.chemgeo.2004.06.017

Jaffey, A.H., Flynn, K.F., Glendenin, L.E., Bentley, W.C., Essling, A.M., 1971. Precision Measurement of Half-Lives and Specific Activities of U 235 and U 238. Phys. Rev. C 4, 1889–1906. https://doi.org/10.1103/PhysRevC.4.1889

Johnston, S., Gehrels, G., Valencia, V., Ruiz, J., 2009. Small-volume U–Pb zircon geochronology by laser ablation-multicollector-ICP-MS. Chemical Geology 259, 218–229. https://doi.org/10.1016/j.chemgeo.2008.11.004

Kay, S.M., Coira, B.L., Caffe, P.J., Chen, C.H., 2010. Regional chemical diversity, crustal and mantle sources and evolution of central Andean Puna plateau ignimbrites. Journal of Volcanology and Geothermal Research 198, 81–111. https://doi.org/10.1016/j.jvolgeores.2010.08.013

Kelly, C.J., McFarlane, C.R.M., Schneider, D.A., Jackson, S.E., 2014. Dating Micrometre-Thin Rims Using a LA - ICP - MS Depth Profiling Technique on Zircon from an Archaean Metasediment: Comparison with the SIMS Depth Profiling Method. Geostandard Geoanalytic Res 38, 389–407. https://doi.org/10.1111/j.1751-908X.2014.00314.x

Kent, A.J.R., Cooper, K.M., 2018. How well do zircons record the thermal evolution of magmatic systems? Geology 46, 111–114. https://doi.org/10.1130/G39690.1

Kern, J.M., de Silva, S.L., Schmitt, A.K., Kaiser, J.F., Iriarte, A.R., Economos, R., 2016. Geochronological imaging of an episodically constructed subvolcanic batholith: U-Pb in zircon chronochemistry of the Altiplano-Puna Volcanic Complex of the Central Andes. Geosphere 12, 1054–1077. https://doi.org/10.1130/GES01258.1

Klepeis, K.A., Crawford, M.L., Gehrels, G., 1998. Structural history of the crustal-scale Coast shear zone north of Portland Canal, southeast Alaska and British Columbia. Journal of Structural Geology 20, 883–904. https://doi.org/10.1016/S0191-8141(98)00020-0

Košler, J., Fonneland, H., Sylvester, P., Tubrett, M., Pedersen, R.-B., 2002. U–Pb dating of detrital zircons for sediment provenance studies—a comparison of laser ablation ICPMS and SIMS techniques. Chemical Geology 182, 605–618. https://doi.org/10.1016/S0009-2541(01)00341-2

Košler, J., Sylvester, P.J., 2003. Present Trends and the Future of Zircon in Geochronology: Laser Ablation ICPMS. Reviews in Mineralogy and Geochemistry 53, 243–275. https://doi.org/10.2113/0530243

Kylander-Clark, A.R.C., 2020. Expanding the limits of laser-ablation U–Pb calcite geochronology. Geochronology 2, 343–354. https://doi.org/10.5194/gchron-2-343-2020

Kylander-Clark, A.R.C., 2017. Petrochronology by Laser-Ablation Inductively Coupled Plasma Mass Spectrometry. Reviews in Mineralogy and Geochemistry 83, 183–198. https://doi.org/10.2138/rmg.2017.83.6

Lambert, D., 1992. Zero-Inflated Poisson Regression, with an Application to Defects in Manufacturing. Technometrics 34, 1. https://doi.org/10.2307/1269547

Lash, T.L., Fox, M.P., Fink, A.K., 2009. Applying Quantitative Bias Analysis to Epidemiologic Data, Statistics for Biology and Health. Springer New York, New York, NY. https://doi.org/10.1007/978-0-387-87959-8

Lewis, C., de Silva, S., Cisneros De Leon, A., Burns, D., Villarroel, M., 2025. Effusive volcanic microcosm of a regional ignimbrite flare-up: Prolonged life cycle of the Chaxas Complex, northern Chile, and its influence on modern volcanic arc character. Geological Society of America Bulletin. https://doi.org/10.1130/B37909.1

Lewis, C., Kent, A., Russo, C., Lubbers, J., 2023. LaserTRAMZ. https://doi.org/10.5281/ZENODO.8097362

Longerich, H.P., Jackson, S.E., Gunther, D., 1996. Laser Ablation Inductively Coupled Plasma Mass Spectrometric Transient Signal Data Acquisition and Analyte

Concentration Calculation*. Journal of Analytical Atomic Spectrometry 11, 899–904.

Lucassen, F., Becchio, R., Harmon, R., Kasemann, S., Franz, G., Trumbull, R., Wilke, H.G., Romer, R.L., Dulski, P., 2001. Composition and density model of the continental crust at an active continental margin - The Central Andes between 21° and 27°S. Tectonophysics 341, 195–223. https://doi.org/10.1016/S0040-1951(01)00188-3

Malusà, M.G., Carter, A., Limoncelli, M., Villa, I.M., Garzanti, E., 2013. Bias in detrital zircon geochronology and thermochronometry. Chemical Geology 359, 90–107. https://doi.org/10.1016/j.chemgeo.2013.09.016

Mattinson, J.M., 1987. U□Pb ages of zircons: A basic examination of error propagation. Chemical Geology: Isotope Geoscience section 66, 151–162. https://doi.org/10.1016/0168-9622(87)90037-6

McLeod, C.L., Davidson, J.P., Nowell, G.M., De Silva, S.L., Schmitt, A.K., 2013. Characterizing the continental basement of the Central Andes: Constraints from Bolivian crustal xenoliths. Geological Society of America Bulletin 125, 985–997. https://doi.org/10.1130/B30721.1

Miller, J.S., Matzel, J.E.P., Miller, C.F., Burgess, S.D., Miller, R.B., 2007. Zircon growth and recycling during the assembly of large, composite arc plutons. Journal of Volcanology and Geothermal Research 167, 282–299. https://doi.org/10.1016/j.jvolgeores.2007.04.019

Mucek, A.E., Danišík, M., De Silva, S.L., Schmitt, A.K., Pratomo, I., Coble, M.A., 2017. Post-supereruption recovery at Toba Caldera. Nat Commun 8, 15248. https://doi.org/10.1038/ncomms15248

Müller, W., Shelley, M., Miller, P., Broude, S., 2009. Initial performance metrics of a new custom-designed ArF excimer LA-ICPMS system coupled to a two-volume laser-ablation cell. J. Anal. At. Spectrom. 24, 209–214. https://doi.org/10.1039/B805995K

National Academies of Sciences, Engineering, and Medicine, 2020. A vision for NSF earth sciences 2020-2030, A Vision for NSF Earth Sciences 2020-2030. National Academies Press. https://doi.org/10.17226/25761

Paces, J.B., Miller, J.D., 1993. Precise U-Pb ages of Duluth Complex and related mafic intrusions, northeastern Minnesota: Geochronological insights to physical, petrogenetic, paleomagnetic, and tectonomagmatic processes associated with the 1.1 Ga Midcontinent Rift System. J. Geophys. Res. 98, 13997–14013. https://doi.org/10.1029/93JB01159

Paton, C., Woodhead, J.D., Hellstrom, J.C., Hergt, J.M., Greig, A., Maas, R., 2010. Improved laser ablation U-Pb zircon geochronology through robust downhole fractionation correction: IMPROVED LASER ABLATION U-Pb GEOCHRONOLOGY. Geochem. Geophys. Geosyst. 11, n/a-n/a. https://doi.org/10.1029/2009GC002618

Pidgeon, R.T., 1992. Recrystallisation of oscillatory zoned zircon: some geochronological and petrological implications. Contrib Mineral Petrol 110, 463–472. https://doi.org/10.1007/BF00344081

Pullen, A., Ibáñez-Mejia, M., Gehrels, G.E., Giesler, D., Pecha, M., 2018. Optimization of a Laser Ablation-Single Collector-Inductively Coupled Plasma-Mass Spectrometer (Thermo Element 2) for Accurate, Precise, and Efficient Zircon U-Th-Pb Geochronology. Geochem. Geophys. Geosyst. 19, 3689–3705. https://doi.org/10.1029/2018GC007889

Ramsey, F., Schafer, D., 2013. The Statistical Sleuth: A Course in Methods of Data Analysis, 3rd ed. Richard Stratton, Brooks/Cole Cangage Learning.

Rivera, T.A., Schmitz, M.D., Jicha, B.R., Crowley, J.L., 2016. Zircon Petrochronology and 40 Ar/ 39Ar Sanidine Dates for the Mesa Falls Tuff: Crystal-scale Records of Magmatic Evolution and the Short Lifespan of a Large Yellowstone Magma Chamber. J. Petrology 1677–1704. https://doi.org/10.1093/petrology/egw053

Rubatto, D., Hermann, J., 2007. Experimental zircon/melt and zircon/garnet trace element partitioning and implications for the geochronology of crustal rocks. Chemical Geology 241, 38–61. https://doi.org/10.1016/j.chemgeo.2007.01.027

Schaen, A.J., Schoene, B., Dufek, J., Singer, B.S., Eddy, M.P., Jicha, B.R., Cottle, J.M., 2021. Transient rhyolite melt extraction to produce a shallow granitic pluton. Sci. Adv. 7, eabf0604. https://doi.org/10.1126/sciadv.abf0604

Schaltegger, U., Schmitt, A.K., Horstwood, M.S.A., 2015. U–Th–Pb zircon geochronology by ID-TIMS, SIMS, and laser ablation ICP-MS: Recipes, interpretations, and opportunities. Chemical Geology 402, 89–110. https://doi.org/10.1016/j.chemgeo.2015.02.028

Schärer, U., 1984. The effect of initial230Th disequilibrium on young UPb ages: the Makalu case, Himalaya. Earth and Planetary Science Letters 67, 191–204. https://doi.org/10.1016/0012-821X(84)90114-6

Schmitt, A.K., Chamberlain, K.R., Swapp, S.M., Harrison, T.M., 2010. In situ U–Pb dating of micro-baddeleyite by secondary ion mass spectrometry. Chemical Geology 269, 386–395. https://doi.org/10.1016/j.chemgeo.2009.10.013

Schmitz, M.D., Bowring, S.A., 2001. U-Pb zircon and titanite systematics of the Fish Canyon Tuff: an assessment of high-precision U-Pb geochronology and its application to young volcanic rocks. Geochimica et Cosmochimica Acta 65, 2571–2587. https://doi.org/10.1016/S0016-7037(01)00616-0

Simonetti, A., Heaman, L.M., Hartlaub, R.P., Creaser, R.A., MacHattie, T.G., Böhm, C., 2005. U–Pb zircon dating by laser ablation-MC-ICP-MS using a new multiple ion counting Faraday collector array. J. Anal. At. Spectrom. 20, 677. https://doi.org/10.1039/b504465k

Sláma, J., Košler, J., 2012. Effects of sampling and mineral separation on accuracy of detrital zircon studies. Geochem. Geophys. Geosyst. 13, Q05007. https://doi.org/10.1029/2012GC004106

Sláma, J., Košler, J., Condon, D.J., Crowley, J.L., Gerdes, A., Hanchar, J.M., Horstwood, M.S.A., Morris, G.A., Nasdala, L., Norberg, N., Schaltegger, U., Schoene, B., Tubrett, M.N., Whitehouse, M.J., 2008. Plešovice zircon — A new natural reference material for U–Pb and Hf isotopic microanalysis. Chemical Geology 249, 1–35. https://doi.org/10.1016/j.chemgeo.2007.11.005

Stern, R.A., Bodorkos, S., Kamo, S.L., Hickman, A.H., Corfu, F., 2009. Measurement of SIMS Instrumental Mass Fractionation of Pb Isotopes During Zircon Dating. Geostandard Geoanalytic Res 33, 145–168. https://doi.org/10.1111/j.1751-908X.2009.00023.x

Tang, D.L.K., Wilson, C.J.N., Sewell, R.J., Seward, D., Chan, L.S., Ireland, T.R., Wooden, J.L., 2017. Tracking the evolution of Late Mesozoic arc-related magmatic systems in Hong Kong using in-situ U-Pb dating and trace element analyses in zircon. American Mineralogist 102, 2190–2219. https://doi.org/10.2138/am-2017-6071

Tavazzani, L., Wotzlaw, J.-F., Economos, R., Sinigoi, S., Demarchi, G., Szymanowski, D., Laurent, O., Bachmann, O., Chelle-Michou, C., 2023. High-precision zircon age spectra record the dynamics and evolution of large open-system silicic magma reservoirs. Earth and Planetary Science Letters 623, 118432. https://doi.org/10.1016/j.epsl.2023.118432

Vanhaecke, F., Degryse, P. (Eds.), 2012. Isotopic Analysis: Fundamentals and Applications Using ICP-MS, 1st ed. Wiley. https://doi.org/10.1002/9783527650484

Vavra, G., 1990. On the kinematics of zircon growth and its petrogenetic significance: a cathodoluminescence study. Contr. Mineral. and Petrol. 106, 90–99. https://doi.org/10.1007/BF00306410

Vavra, G., Schmid, R., Gebauer, D., 1999. Internal morphology, habit and U-Th-Pb microanalysis of amphibolite-to-granulite facies zircons: geochronology of the Ivrea Zone (Southern Alps). Contributions to Mineralogy and Petrology 134, 380–404. https://doi.org/10.1007/s004100050492

Vermeesch, P., 2021. Maximum depositional age estimation revisited. Geoscience Frontiers 12, 843–850. https://doi.org/10.1016/j.gsf.2020.08.008

Vermeesch, P., 2018. IsoplotR: A free and open toolbox for geochronology. Geoscience Frontiers 9, 1479–1493. https://doi.org/10.1016/j.gsf.2018.04.001

Weber, G., Caricchi, L., Arce, J.L., Schmitt, A.K., 2020. Determining the current size and state of subvolcanic magma reservoirs. Nature Communications 11. https://doi.org/10.1038/s41467-020-19084-2

Wiedenbeck, M., Allé, P., Corfu, F., Griffin, W.L., Meier, M., Oberli, F., Quadt, A.V., Roddick, J.C., Spiegel, W., 1995. THREE NATURAL ZIRCON STANDARDS FOR U-TH-PB, LU-HF, TRACE ELEMENT AND REE ANALYSES. Geostandards and Geoanalytical Research 19, 1–23. https://doi.org/10.1111/j.1751-908X.1995.tb00147.x

Fig. 1

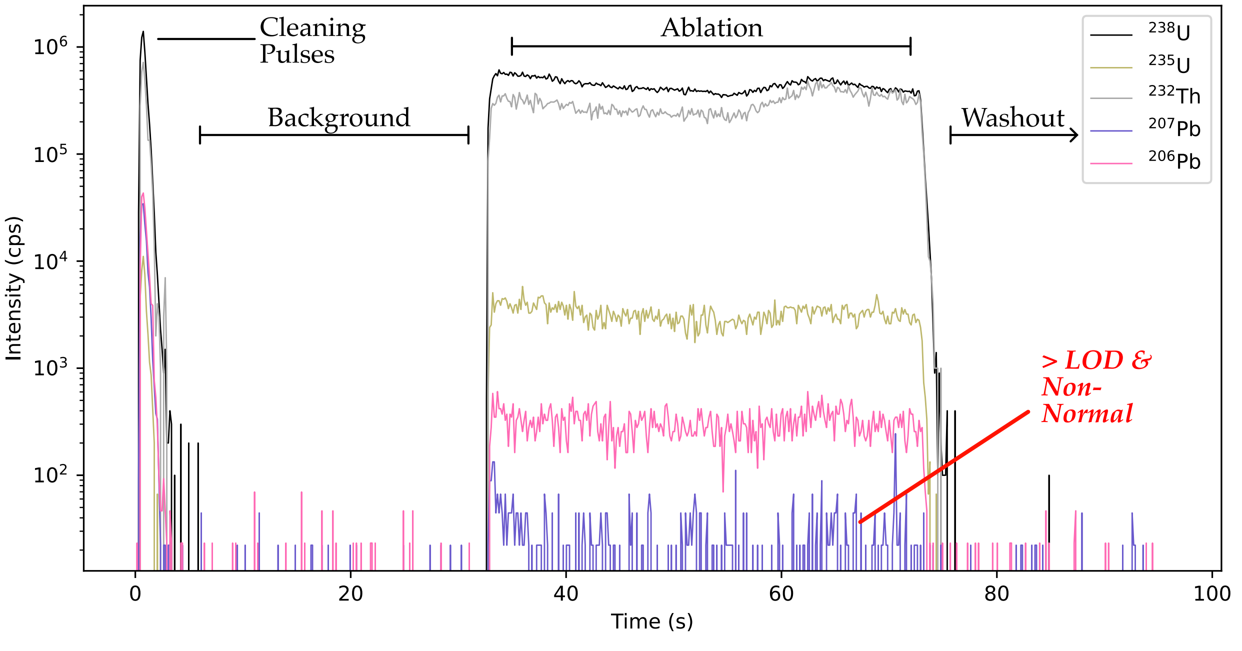
Cleaning Pulses
Background
Ablation
Washout
> LOD & Non-Normal
^{238}U
^{235}U
^{232}Th
^{207}Pb
^{206}Pb
Intensity (cps)
Time (s)
10^2
10^3
10^4
10^5
10^6
0
20
40
60
80
100

Fig. 2

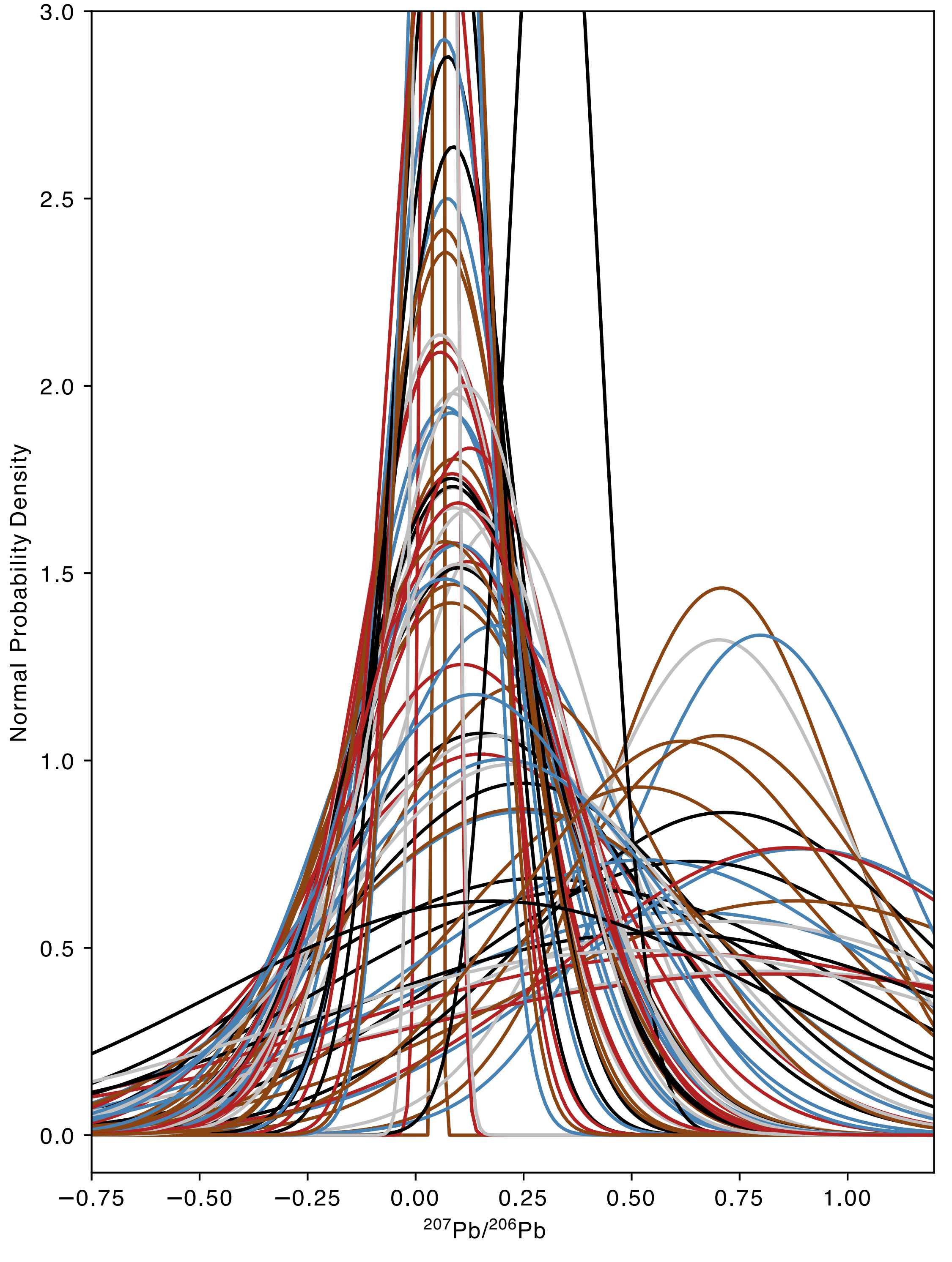
3.0
2.5
2.0
1.5
1.0
0.5
0.0
Normal Probability Density
−0.75
−0.50
−0.25
0.00
0.25
0.50
0.75
1.00
207Pb/206Pb

Fig. 3

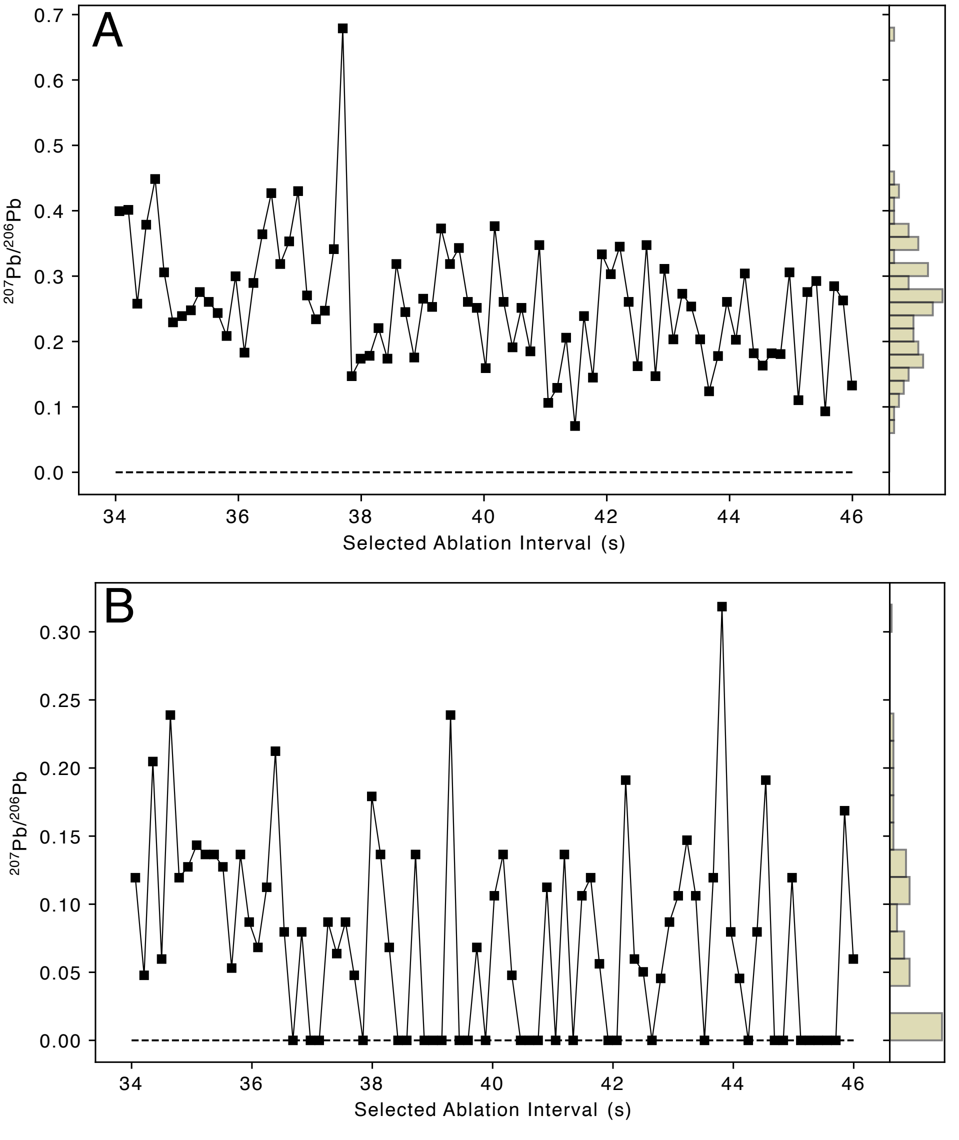
A
B
$^{207}Pb/^{206}Pb$
Selected Ablation Interval (s)
0.0
0.1
0.2
0.3
0.4
0.5
0.6
0.7
0.00
0.05
0.10
0.15
0.20
0.25
0.30
34
36
38
40
42
44
46

Fig. 4

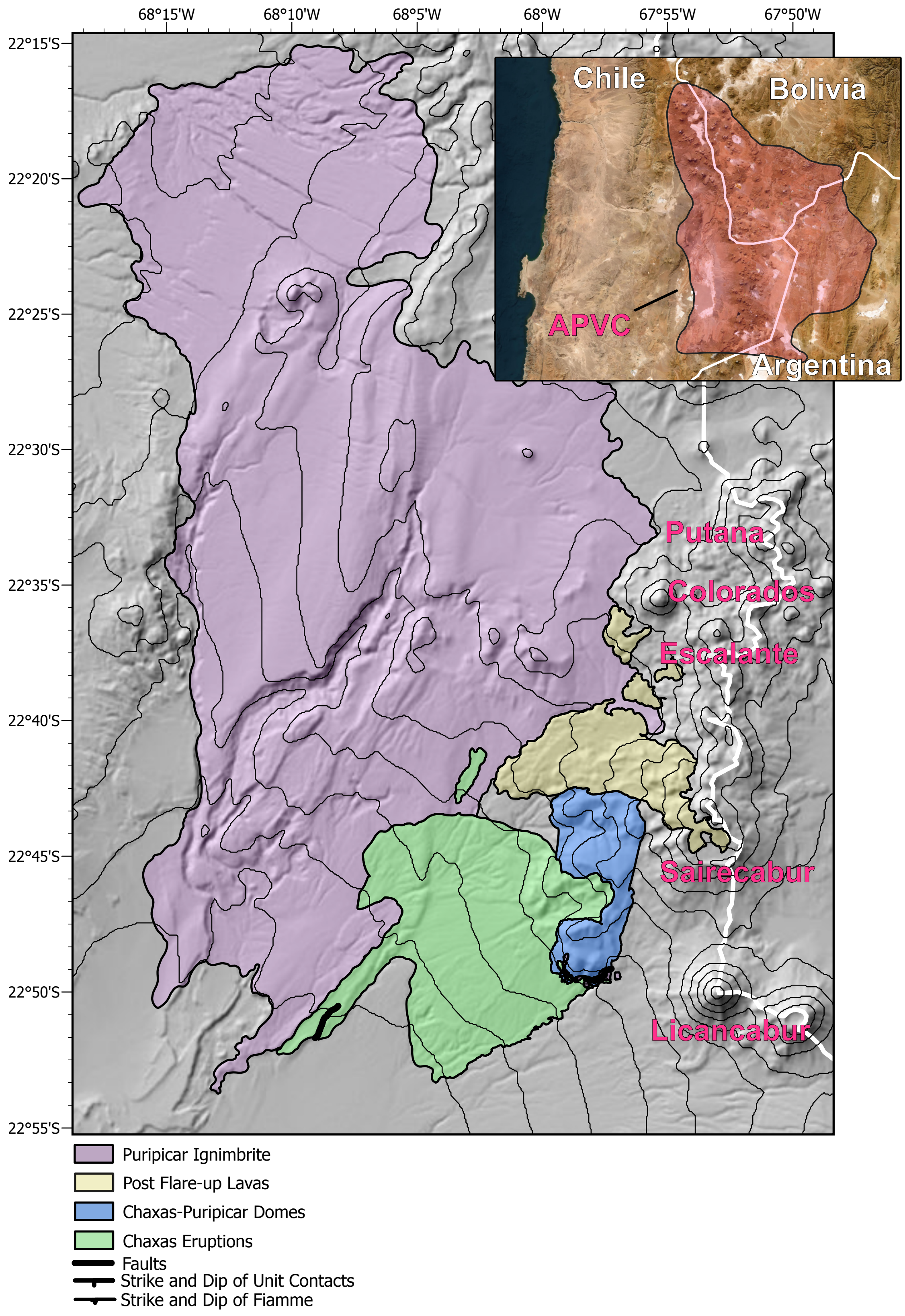
68°15'W
68°10'W
68°5'W
68°W
67°55'W
67°50'W
22°15'S
22°20'S
22°25'S
22°30'S
22°35'S
22°40'S
22°45'S
22°50'S
22°55'S
Chile
Bolivia
APVC
Argentina
Putana
Colorados
Escalante
Sairecabur
Licancabur
Puripicar Ignimbrite
Post Flare-up Lavas
Chaxas-Puripicar Domes
Chaxas Eruptions
Faults
Strike and Dip of Unit Contacts
Strike and Dip of Fiamme

Fig. 5

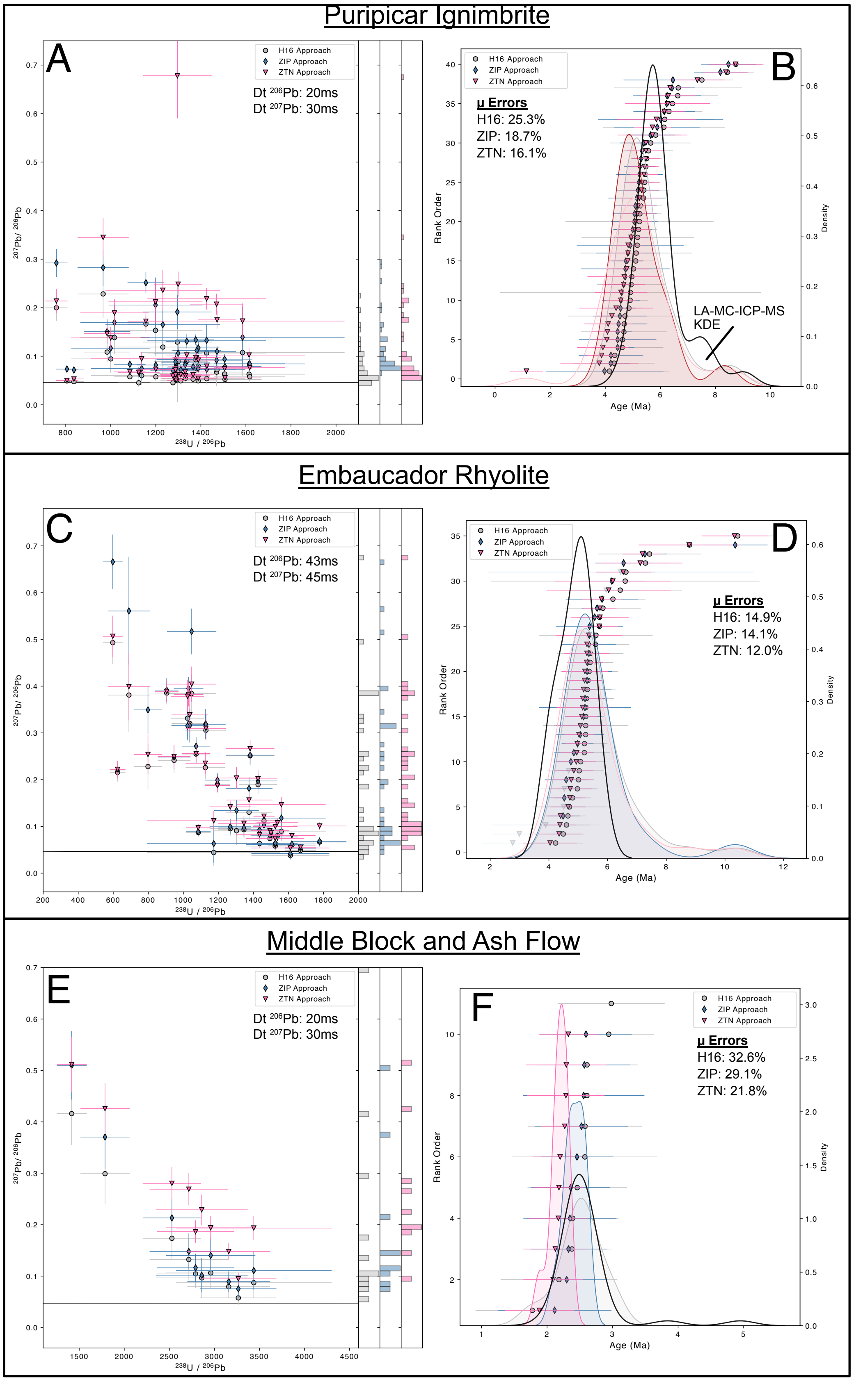

Puripicar Ignimbrite
A
H16 Approach
ZIP Approach
ZTN Approach
Dt 206Pb: 20ms
Dt 207Pb: 30ms
207Pb/ 206Pb
238U / 206Pb
B
µ Errors
H16: 25.3%
ZIP: 18.7%
ZTN: 16.1%
LA-MC-ICP-MS
KDE
Rank Order
Density
Age (Ma)
Embaucador Rhyolite
C
Dt 206Pb: 43ms
Dt 207Pb: 45ms
D
µ Errors
H16: 14.9%
ZIP: 14.1%
ZTN: 12.0%
Middle Block and Ash Flow
E
Dt 206Pb: 20ms
Dt 207Pb: 30ms
F
µ Errors
H16: 32.6%
ZIP: 29.1%
ZTN: 21.8%

Fig. 6

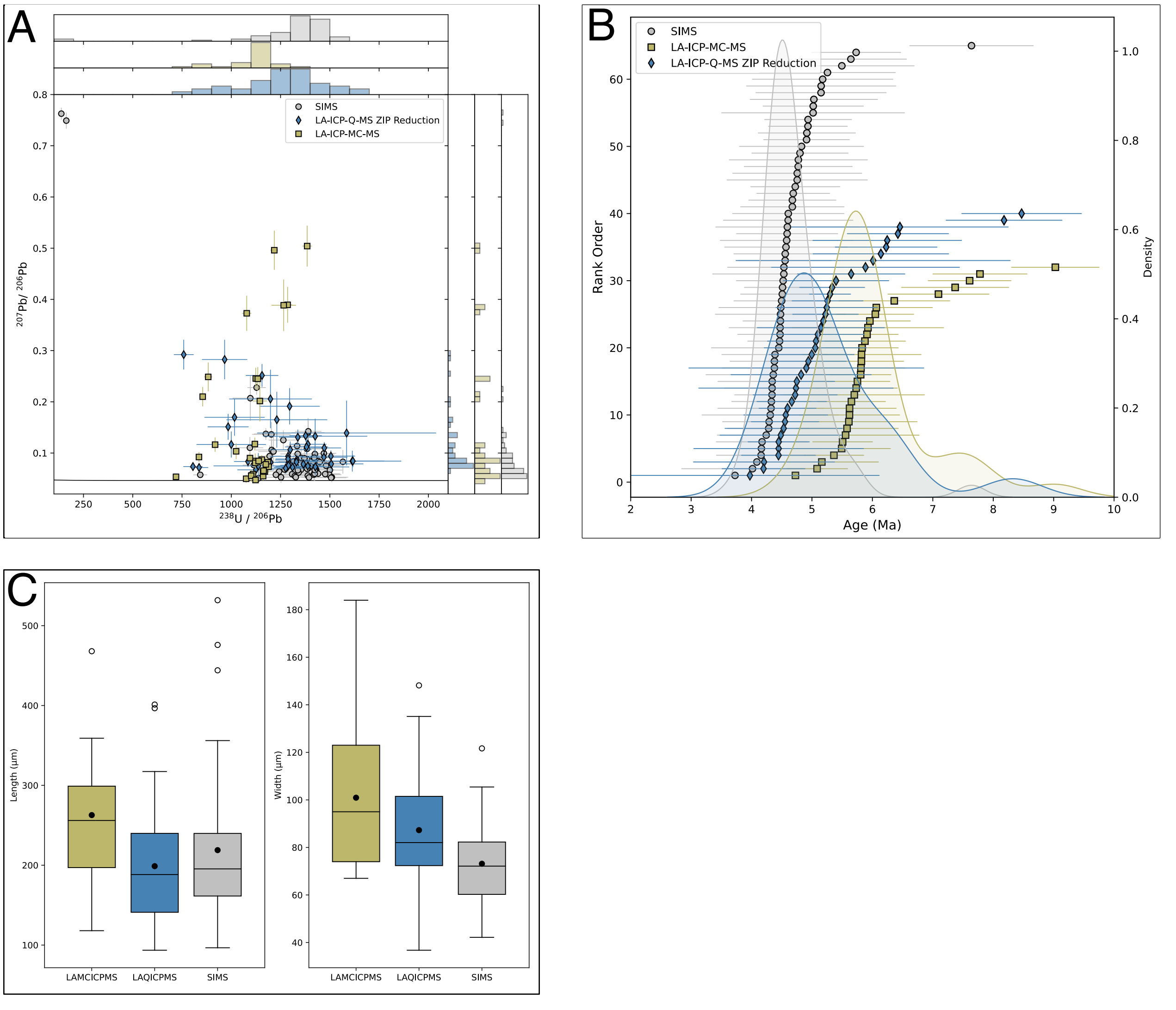
A
SIMS
LA-ICP-Q-MS ZIP Reduction
LA-ICP-MC-MS
^{207}Pb/ ^{206}Pb
^{238}U / ^{206}Pb
B
SIMS
LA-ICP-MC-MS
LA-ICP-Q-MS ZIP Reduction
Rank Order
Density
Age (Ma)
C
Length (μm)
Width (μm)
LAMCICPMS
LAQICPMS
SIMS

Fig. 7

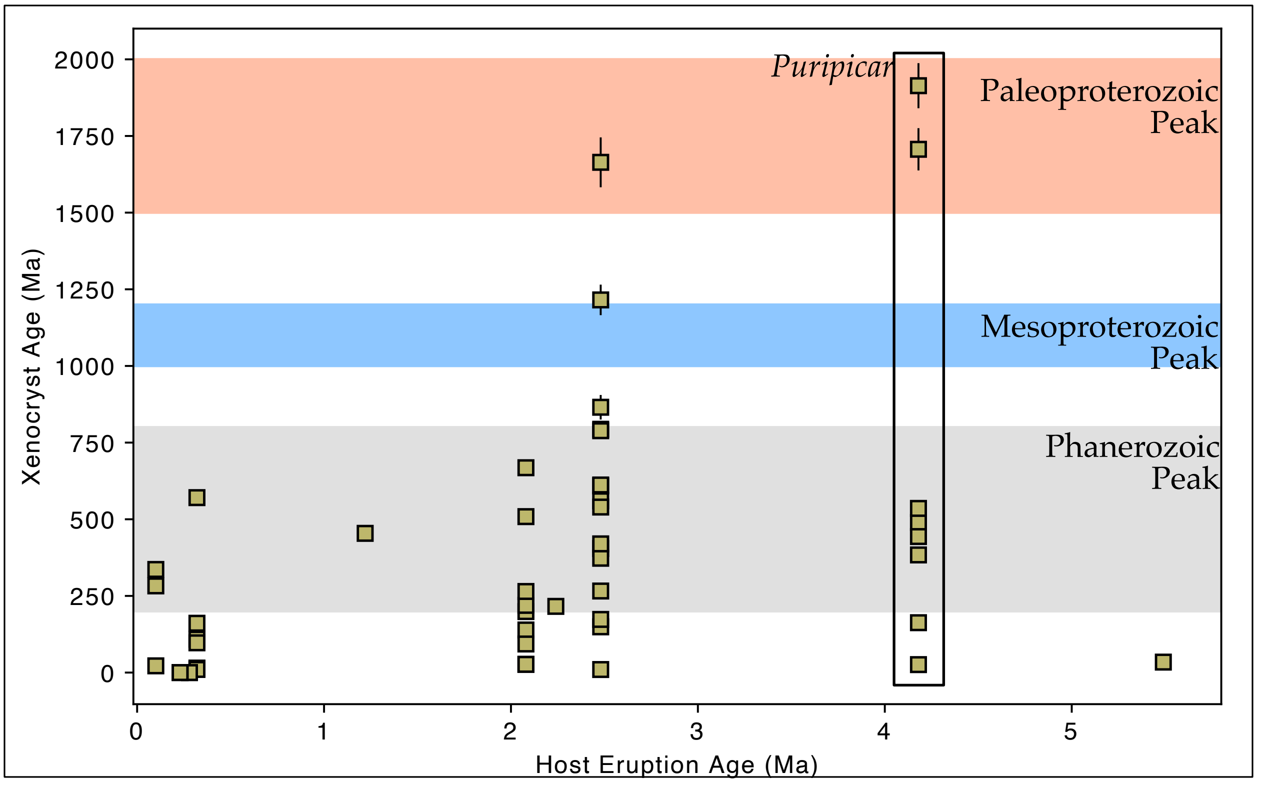

Xenocryst Age (Ma)
2000
1750
1500
1250
1000
750
500
250
0
Puripicar
Paleoproterozoic Peak
Mesoproterozoic Peak
Phanerozoic Peak
0
1
2
3
4
5
Host Eruption Age (Ma)

Fig. 8

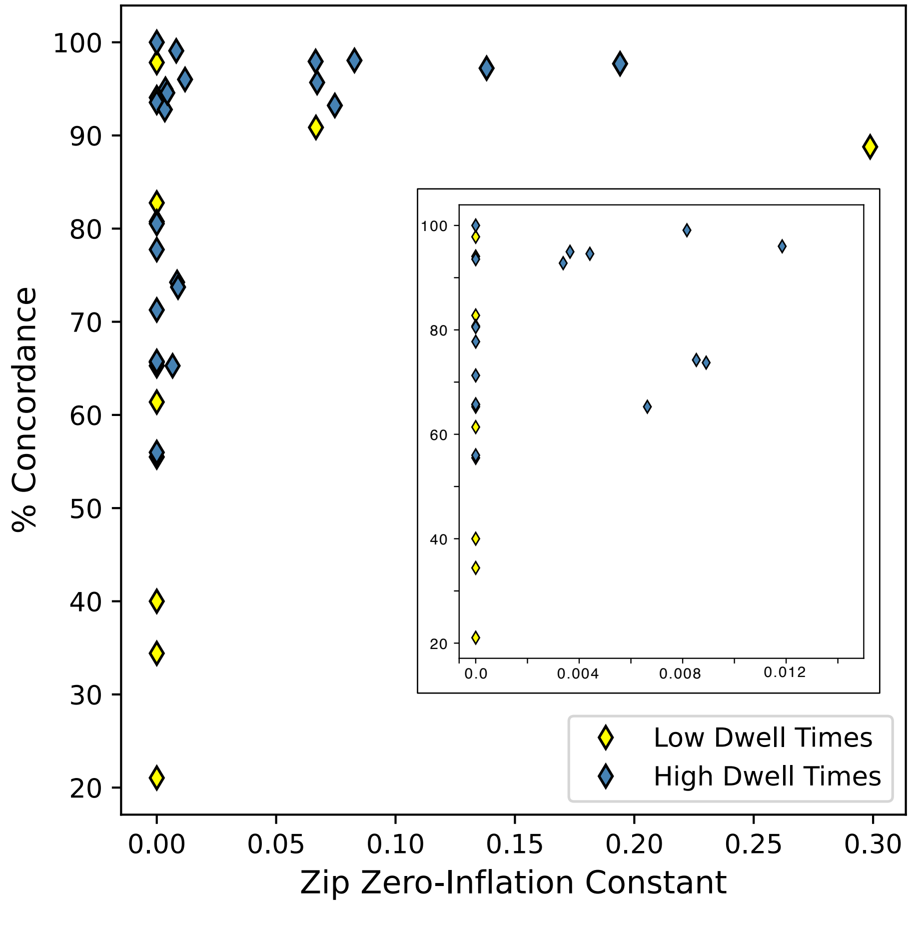
100
90
80
70
60
50
40
30
20
% Concordance
0.00
0.05
0.10
0.15
0.20
0.25
0.30
Zip Zero-Inflation Constant
Low Dwell Times
High Dwell Times
0.0
0.004
0.008
0.012

Fig. 9

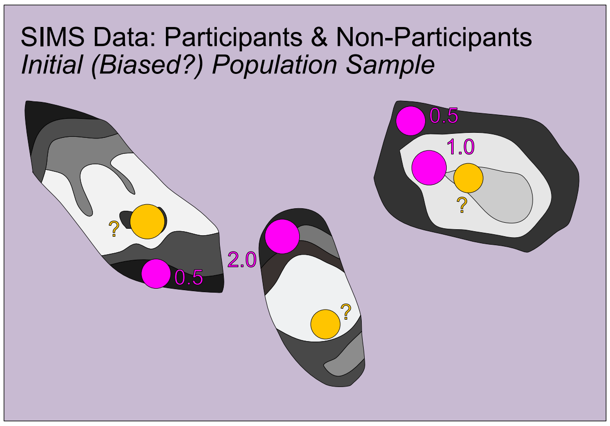

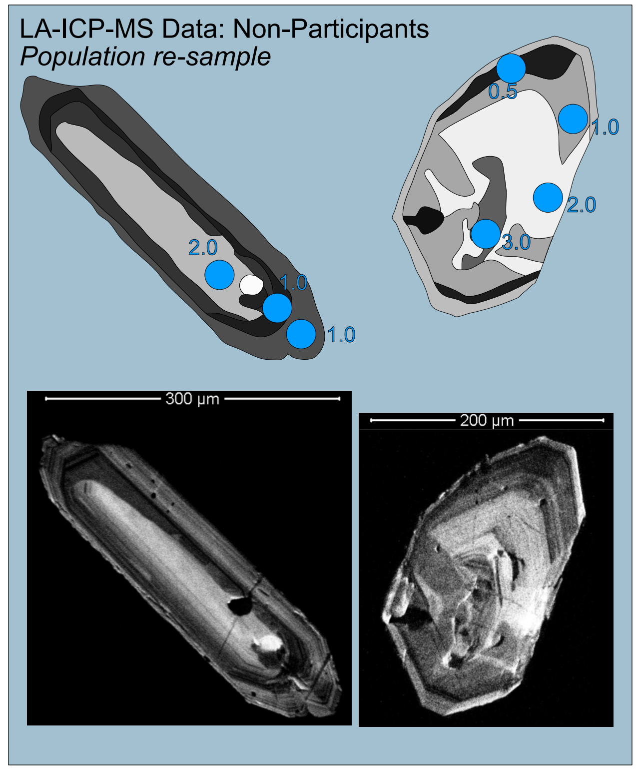

Characterized Non-Participants Pop. (Bias Check)
Hypothetical Spot & Age

Initial Participants Pop. (Biased?)
Hypothetical Spot & Age

Non-Participants Pop. (Neglected by Bias)
Hypothetical Spot & Age

	Participants Pop.		Characterized Non-Participants Pop.		Non-Participants
	Old Age	Young Age	Old Age	Young Age	-
Core/Interior	0	1	2	1	3
Rim	1	2	1	3	0
Odds of Seeing Old Age in Core	**0**		**6**		**?**
Bias Indicated! Adjust Assuming Non-Participants = Bias Check Pop.					
Adjusted Odds of Seeing Old Age in Core	**3.33**				
Missing Population Characterized - Inferred Bias Likely					

Table 1: Comparison of in-situ MS Characteristics			
	LA-Q-ICP-MS^	**LA-MC-ICP-MS**	**SIMS**
Precision (%)	0.1	2%	1-2 %
Spatial Resolution	OK	Good	Great
Useful Yield (Pb; %)	≤ 0.01 %	2%	1%
Useful Yield (U; %)	≤ 0.01 %	2.8%	1-2%
Instrument Cost (Mil. USD)	0.5	1	≥ 4
Analytical Cost / Day (USD)	< 1000	1000-1500	1800 - 4000
Analysis Time	≤ 2 Minutes	≤ 2 Minutes	10-20 Minutes
Sample Prep Time	Days - Weeks	Days - Weeks	Days - Weeks

^ Non-Magnetic Sector. see Schmitt et al. (2010); Frei and Gerdes (2009); Cottle et al. (2009); Schaltegger et al. (2015) for additional detail

Table 2: Metadata and Standardization Information for LA-ICP-MS U-Pb Dates		
Lab and Sample Preparation		
Lab & University	W.M. Keck Collaboraty, Oregon State University	
Sample Type	Pumice	
Mineral Separation	Mortar and Pestle + Gold Pan	
Mineral Mounting	1" Epoxy resin polished to 1µm	
Imaging	CL with FEI Quanta 600F. 15kV voltage, 10µm working distance, 4µm spot	
Laser Ablation Instrument and Settings		
Make / Model	Applied Spectra RESOlution SE	
Ablation Cell	Laurin Technic S155	
Wavelength / Pulse Width	193nm / 5ns	
Fluence	~3.5 J cm^{-2}	
Pulse Rate	5 Hz	
Spot Diameter	30 µm	
Carrier Gas	He in cell. Ar mixed at top of He funnel during sample extraction	
Carrier Gas Flow Rate	650 ml min^{-1} He	
ICP-MS Instrumentation		
	Q-ICP-MS	*MC-ICP-MS*
Make / Model	ThermoFisher iCAP RQ	Nu Plasma3D
Detection System	Analog & Ion Counting Single Collection	Faradays (238U, 235U, 232Th), Daly Photomultipliers (208-206Pb), and Ion Counters (204Pb and 202Hg)
Measured Masses (Integration Times)	202 (0.01), 204(0.01), 206(0.043), 207(0.045), 208(0.001), 232(0.001), 235(0.015), 238(0.01)	0.1s on all masses
Data Processing		
Software Package	LaserTRAMZ	
Ablation Site U - Pb Fractionation	Exponential Regression	
Intrumental Mass Fractionation	EFF	238U/235U: Exponential correction using 137.818. 238U/232Th: EFF. Pb/U: EFF. Pb/Pb: EFF
Standardization	Primary: Temora-2. Secondary: PlasmAge Standards	Primary: Temora-2. Secondary: 91500, 94-35, Plesovice
Standard Reproducibility / Uncertainty^	1-10% / 2-15%	0.2-1% / 0.5 - 3%

EFF: Empirical Fractionation Factor

^Expressed as offset from accepted value / Uncertainty on single age of secondary standard reference materials

Table 3: Collector Block and Detection Limits for the Nu Plasma 3D								
Detector #	**H10**	**H9**	**H7**	**D0**	**D1**	**D2**	**IC3**	**IC4**
Detector Type	Faraday	Faraday	Faraday	Daly	Daly	Daly	Ion Counter	Ion Counter
Isotopes	238U	235U	232Th	208Pb	207Pb	206Pb	204Pb	202Hg
DL (cps)	5700	6900	6130	410	280	280	90	1

Table 4: Summary of reduction methods and pertinent details										
Unit	**Dwell Times**		**% Concordance**			**$^{207}Pb/^{206}Pb$ % Error (2SE)^**			**Age % Error (2SE)+**		
	Dt 207Pb	Dt 206Pb	H16	ZIP	ZTN	H16	ZIP	ZTN	H16	ZIP	ZTN
Puripicar	0.3	0.2	95.3	91.1	89.4	19.1	13.9	9.3	25.3	18.7	16.1
Embaucador Rhyolite*	0.45	0.43	94.5	94.1	92.2	12.5	11.5	8.8	14.9	14.1	12.0
Middle Block and Ash	0.3	0.2	80.8	82.1	73.8	24.5	17.9	9.8	32.6	29.1	21.8

*Considering High dwell time data; ^does not include excess variance; +includes excess variance

Table 5: Crude Odds Ratios		
Crude Odds Associations	**SIMS**	**LAQICPMS**
Cores and Old Ages	0.07	1.07
Cores with Bright Zones	0.48	2.33

Table 6: Odds and Adjusted Odds for combining spatial and age assocations					
	SIMS		LAICPMS		SIMS Non-Participants
	Old Age	No Old Age	Old Age	No Old Age	
Bright Core	0	15	3	3	7
Not Bright Core	2	33	7	32	48
Odds of Seeing Bright Core with Old Age	*0*		*4.6*		
Adjusted Odds of seeing Bright Core with Old Age	**1.80**				

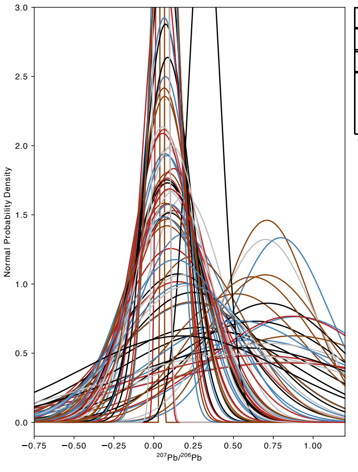

Table 4: Summary of reduction methods and pertinent details												
Unit	Dwell Times		% Concordance			$^{207}Pb/^{206}Pb$% Error (2SE)^			Age % Error (2SE)+		
	Dt 207Pb	Dt 206Pb	H16	ZIP	ZTN	H16	ZIP	ZTN	H16	ZIP	ZTN
Puripicar	0.3	0.2	95.3	91.1	89.4	19.1	13.9	9.3	25.3	18.7	16.1
Embaucador Rhyolite*	0.45	0.43	94.5	94.1	92.2	12.5	11.5	8.8	14.9	14.1	12.0
Middle Block and Ash	0.3	0.2	80.8	82.1	73.8	24.5	17.9	9.8	32.6	29.1	21.8

*Considering High dwell time data; ^does not include excess variance; +includes excess variance

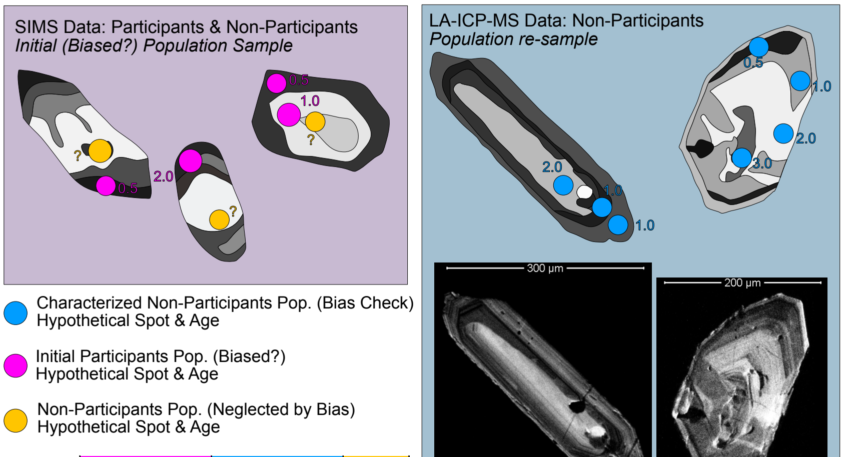

	Participants Pop.		Characterized Non-Participants Pop.		Non-Participants
	Old Age	Young Age	Old Age	Young Age	-
Core/Interior	0	1	2	1	3
Rim	1	2	1	3	0
Odds of Seeing Old Age in Core	**0**		**6**		**?**
Bias Indicated! Adjust Assuming Non-Participants = Bias Check Pop.					
Adjusted Odds of Seeing Old Age in Core	**3.33**				

Missing Population Characterized - Inferred Bias Likely

1. A new approach to the reduction of the $^{207}Pb/^{206}Pb$ ratio in U-Pb zircon measurements is presented for the specific case of conducting measurements using a quadrupole ICP-MS when dating young (< 10 Ma) crystals.

2. Precision on the $^{207}Pb/^{206}Pb$ ratio is improved by 1 – 7 % with differences in concordance being within the error of the determined ratios.

3. Age bias in zircon datasets collected from the same rocks in two different studies is quantified using Quantitative Bias methodology to show the magnitude of bias induced by the analyst during spot selection guided by CL-images.

Dampening of Oscillations

Oscillations in LA-ICP-MS analyses are detrimental to accurate determination of ratios. These may be generated by either aliasing of the duty cycle with the laser pulse rate, or, a rapid signal decay induced by fast ablation cell washout. For the RESOlution-SE the latter is pertinent and a signal smoothing device (aka, "squid") is frequently used. However, these devices are commonly annoying due to the introduction of a possible contaminant source by using more total sample carrier line and prolonged purging periods required before plasma start-up. We chose to simply add 3m of nylon line to the sample carrier gas to increase the washout time and smooth the signal.

Time-series analysis can directly test the efficacy of our rather simple solution (Ramsey and Schafer 2013). Steps to implement the test are as follows:

1) Take the residuals of a regression line through the 206Pb/238U ratio for a selected ablation duration. Call these the i residulas.

2) Remove the first duty cycle and take the regressions. Call these the i+1 residuals.

3) Recognize that if oscillations are present, the residuals for the i^{th} pass will be opposed about the regression line relative to the j^{th} pass ($j > i$). That is, the residual at the i^{th} pass will have the opposite sign of the j^{th} pass because oscillation in the 206Pb/238U ratios result in values on either side of the regression line.

4) Plot the i+1 residuals versus the i residuals and test for correlation. If no correlation is present, then oscillations have been successfully dampened. The graph below shows two analyses of the same crystal, one without the 3m of line and one with, to demonstrate the efficacy of simply adding additional line.

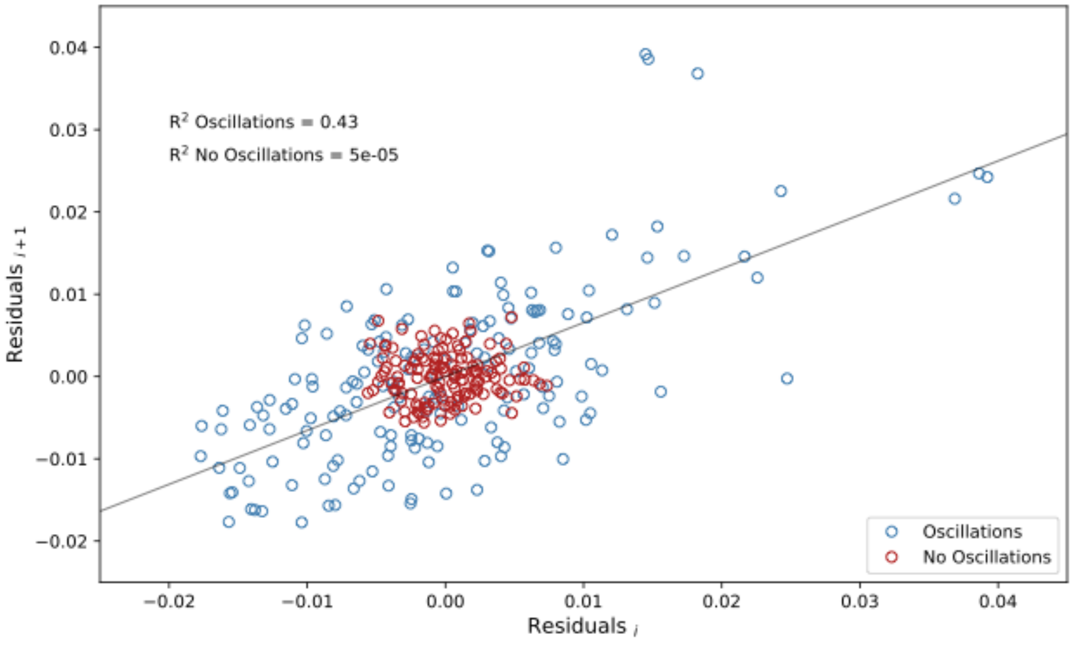

R² Oscillations = 0.43
R² No Oscillations = 5e-05
Residuals i+1
Residuals i
Oscillations
No Oscillations
0.04
0.03
0.02
0.01
0.00
−0.01
−0.02
−0.02
−0.01
0.00
0.01
0.02
0.03
0.04

Pb Isotope Solutions Column Chemistry and MC-ICPMS Methodology

Mass of plagioclase required to get 40ng of Pb from upper crustal silicic magmas in the Central Andes of Chile was estimated based on prior measurements of Pb concentrations in feldspar in the Keck lab (Lubbers et al. 2022), resulting in an estimate of 15-20 mg. Inclusion free grains were picked from a petri-dish filled with DI. Cross-polarizers were used with partial extinction to help identify inclusions. Separates were then weighed in 15 mL Savillex® beakers. Grains were digested in 4mL of 3:1 HF:HNO_3 on a hotplate then dried down once in solution. Samples were then brought up in concentrated nitric and dried down again to be put into 1N HBr and put through Pb column chemistry.

AG1-x8 Cl- form resin was used for elemental separation using well-established column calibrations at OSU. HCl and Milli-Q cleaning steps were first implemented to elute any contaminant Pb and rinse the column. Resin was then conditioned with 1N HBr, then samples were loaded onto columns. Pb was then isolated using a series of HBr steps, followed by 2N HCl to elute Br- and convert the resin environment to HCl. Pb cuts were then eluted with 6N HCl. Samples were then dried down and underwent a second pass through columns of smaller volume to further purify Pb cuts. Samples were then dried down for a final time and brought up in 2mL of 2% HNO_3 for measurement.

Pb isotope ratios were measured in duplicate on a Nu Plasma 3D at OSU using a sample-standard bracketing approach. Tuning was done on NBS981. After tuning a concentration test of all unknowns was run using 25 µL unknown solutions pipetted into 975 mL of 2% HNO3 along with measurement of NBS981 solution of known concentration to determine the amount of sample solution needed to achieve the same relative sensitivity observed during tuning. Mass bias was achieved using an exponential mass bias factor and NBS981 as a primary standard. ^{202}Hg was monitored to correct for the isobaric interference of 204Hg on ^{204}Pb but no ^{202}Hg was actually detected. Secondary standards include measurement of BHVO-2 and GSP-2 and both were reproduced within error of their accepted values (Weis et al. 2006). Long term reproducibility of these standards in the Keck Collaboratory is on the same order of magnitude as their accepted values (1e-2 – 1e-3; Weis et al. 2006). Values reported here are the weighted mean of duplicate measurements. Errors include the standard deviation of the duplicate measurements and the reproducibility of the secondary standards.

MBA MC Data

As discussed in the text and presented in the reported data in the additional supplementary file the MC and Q data for MBA are underdispersed. Below is a rank-order graph depicting the data.

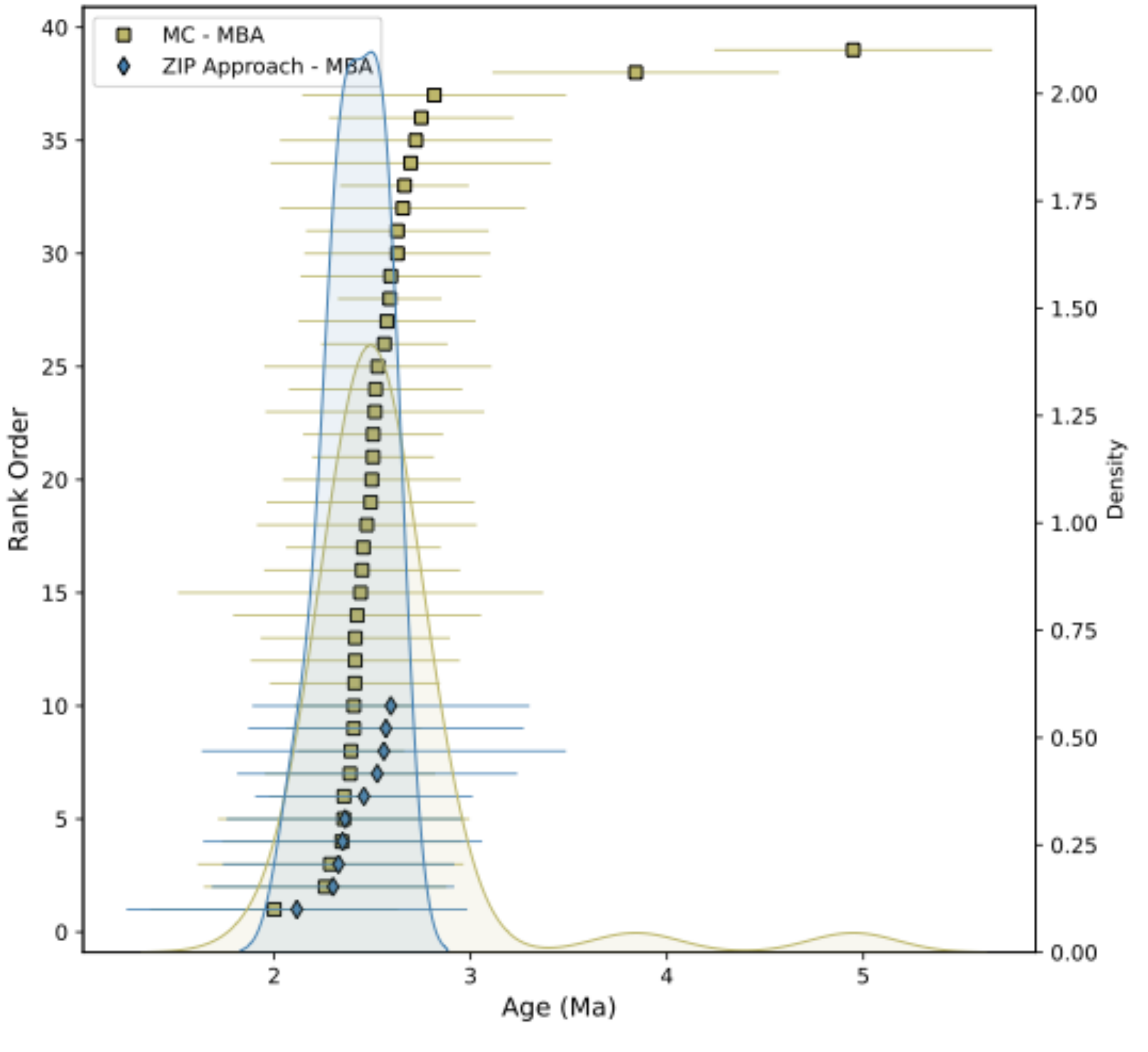

<u>Example Calculation for Quantitative Bias</u>

Lash et al. (2009) describe the numerous issues related to bias in epidemiologic studies. One critical issue in this field is selection bias, or the bias associated with subjects choosing to (or not to) participate in a study due to their relative exposure to some issue. The initially sampled population is referred to as the participants. Naturally there will be refusals for participation and these subjects are referred to as the non-participants. Nevertheless it is of interest to calculate the odds of an association between the population of interest and some phenomenon (e.g., cancer rates) using a basic contingency table of the data gathered from the initial participants.

In most cases it is extremely likely that participants will have been effected by some issue of interest to the epidemiologist (e.g., cancer studies in populations surrounding superfund sites) whereas non-participants will simply not engage. Knowing this bias is present, the population is sampled a second-time but with a less involved participation requirement (e.g., answering a shorter questionnaire). These subjects are considered characterized non-participants. Using a series of odds ratios (percentages) and a series of algebraic equations (see below), one can adjust the odds of the initial participants to account for the non-participants. Typically the epidemiologist has no information regarding which of the non-participants are cases vs controls (the *rows* in the contingency table below) and more sophisticated effort is needed to approximate this information. However, geologic studies benefit from predictable crystal growth (core-to-rim growth) and textural information from images (e.g., CL-images) that can serve as case vs control for the non-participants. An example calculation is in the table below. Classified CL-images are in Supplementy File 2.

Contingency Table Example	Association of Interest ('Old Age')	Not Assocation of Interest (Not Old)	Catagorized Assocation of Non-Participants	Catagorized Non-Assocation of Non-Participants	Uncatogorized Non-Participants
Case (CL-Dark)	x	k	i	g	p
Control (CL-Bright/Gray)	y	m	j	h	q

Crude Odds Ratio $= \dfrac{x/y}{k/m}$ Multiplicative difference of seeing an old age in a CL-dark zone, relative to an old age in another zone

>1: Strong Association with Case
1: Equal Odds between Case and Assocations
<1: No Association with Case

Adjusted Odds Ratio $= \dfrac{\dfrac{x+i+\frac{i}{i+g}p}{y+j+\frac{j}{j+h}q}}{\dfrac{k+g+\frac{g}{i+g}p}{m+h+\frac{h}{j+h}q}}$

Odds of seeing an old age in a CL-dark zone after adjusting for bias introduced from non-participants (categorized and uncatagorized)

Odds of seeing an old age in a CL-bright or gray zone after adjusting for bias introduced from non-participants (categorized and uncatagorized)

Multiplicative difference of seeing an old age in a CL-dark zone relative to an old age in another zone, after adjusting for bias

Odds Ratio:	SIMS	LA-ICP-Q-MS	Adjusted Odds Ratio (SIMS)	
Rim Analyses with Old Ages	14.67	0.74	Bright or Gray Core with Old Age	4.3
Core Analyses with Old Ages	0.45	2.08		
Core Analysis with Dark Zone	3.21	0.95		
Dark Zone with Young Age	3.92	3.29		
Bright or Gray Core with Old Age	0	7.11		

Metadata			Data used for Correction of Isotope Ratios			Measured Isotope Ratios					Corrected 238U/206Pb Ratios & Age		
Unit	Crystal	Spot Number	Common 207Pb/206Pb	Common 207Pb/206Pb 2s	fraction Pbc	238U/206Pb	238U/206Pb 2s %	207Pb/206Pb	207Pb/206Pb 2s %	rho	238U/206Pb c	206Pb/238U Age (Ma)	206Pb/238U Age 2s %
PPI	1	1	0.83279	0.00035	0.03	1469.7	8.0	0.1	43.2	-0.01	1367.0	4.7	43.8
PPI	1	2	0.83279	0.00035	0.02	1614.0	15.3	0.1	30.8	0.00	1490.6	4.3	33.9
PPI	2	1	0.83279	0.00035	0.20	758.6	6.5	0.2	13.3	-0.03	858.4	7.5	15.2
PPI	2	2	0.83279	0.00035	0.14	1198.7	17.4	0.2	35.0	-0.13	1257.5	5.1	39.6
PPI	4	1	0.83279	0.00035	0.08	1585.1	28.6	0.1	44.1	-0.07	1552.8	4.2	52.3
PPI	4	2	0.83279	0.00035	0.08	1425.5	18.4	0.1	26.8	-0.02	1397.2	4.6	32.4
PPI	5	1	0.83279	0.00035	0.04	1388.6	6.7	0.1	11.2	0.00	1314.1	4.9	12.9
PPI	5	2	0.83279	0.00035	0.06	1337.5	7.0	0.1	11.1	-0.01	1282.5	5.0	13.0
PPI	5	3	0.83279	0.00035	0.03	1471.8	5.7	0.1	32.7	0.00	1377.8	4.7	33.2
PPI	6	1	0.83279	0.00035	0.04	1381.6	7.8	0.1	14.5	0.00	1298.2	5.0	16.3
PPI	6	2	0.83279	0.00035	0.02	1331.8	8.1	0.1	12.9	0.00	1225.8	5.3	14.9
PPI	7	1	0.83279	0.00035	0.01	1290.3	5.4	0.1	9.4	0.00	1182.0	5.5	10.6
PPI	7	2	0.83279	0.00035	0.23	966.2	11.8	0.2	22.0	0.26	1141.2	5.6	26.0
PPI	8	1	0.83279	0.00035	0.08	984.0	10.4	0.1	19.5	-0.26	971.7	6.6	22.1
PPI	8	2	0.83279	0.00035	0.01	1426.4	12.0	0.1	22.5	-0.01	1304.7	4.9	25.0
PPI	11	1	0.83279	0.00035	0.02	1505.4	8.1	0.1	11.7	0.00	1392.7	4.6	13.9
PPI	11	2	0.83279	0.00035	0.06	1377.1	5.9	0.1	8.6	0.00	1325.9	4.9	10.3
PPI	12	1	0.83279	0.00035	0.00	1286.4	4.7	0.0	9.3	0.00	1171.9	5.5	10.2
PPI	12	2	0.83279	0.00035	0.00	1124.3	8.2	0.0	17.6	-0.04	1020.6	6.3	19.2
PPI	13	1	0.83279	0.00035	0.00	1276.1	7.9	0.0	14.2	0.00	1156.9	5.6	15.9
PPI	13	2	0.83279	0.00035	0.15	1155.9	7.0	0.2	10.2	0.03	1236.7	5.2	12.7
PPI	14	1	0.83279	0.00035	0.12	1016.4	14.9	0.1	24.7	0.02	1046.2	6.2	29.2
PPI	15	1	0.83279	0.00035	0.00	1310.7	7.1	0.0	15.5	-0.02	1193.7	5.4	16.9
PPI	15	2	0.83279	0.00035	0.11	1295.8	11.7	0.1	95.6	0.02	1312.1	4.9	96.4
PPI	16	1	0.83279	0.00035	0.01	1330.7	7.8	0.1	13.1	0.00	1219.4	5.3	14.9
PPI	16	2	0.83279	0.00035	0.01	1365.6	6.9	0.1	12.5	0.00	1248.1	5.2	14.0
PPI	17	1	0.83279	0.00035	0.05	1299.1	8.2	0.1	38.6	0.05	1245.4	5.2	39.4
PPI	18	1	0.83279	0.00035	0.02	1287.8	6.6	0.1	12.5	0.00	1196.3	5.4	14.0
PPI	19	2	0.83279	0.00035	0.09	1231.0	20.7	0.1	46.8	-88.32	1229.6	5.2	51.3
PPI	20	1	0.83279	0.00035	0.00	1388.0	6.0	0.0	11.5	0.00	1263.0	5.1	12.8
PPI	20	2	0.83279	0.00035	0.01	1507.1	10.7	0.1	15.6	0.00	1374.5	4.7	18.5
PPI	22	2	0.83279	0.00035	0.01	1084.8	6.4	0.1	12.5	0.00	1000.7	6.4	13.9
PPI	23	1	0.83279	0.00035	0.02	1137.1	19.8	0.1	30.9	0.58	1051.7	6.1	36.0
PPI	23	2	0.83279	0.00035	0.06	999.8	17.5	0.1	30.5	0.03	968.6	6.7	34.9
PPI	25	1	0.83279	0.00035	0.00	805.5	5.9	0.0	10.3	0.00	737.1	8.7	11.7
PPI	25	2	0.83279	0.00035	0.00	836.5	5.4	0.0	10.4	0.00	763.9	8.4	11.5
PPI	26	1	0.83279	0.00035	0.02	1287.8	4.8	0.1	9.1	0.01	1186.1	5.4	10.2
PPI	26	2	0.83279	0.00035	0.01	1290.4	3.1	0.1	5.4	0.00	1177.1	5.5	6.1
PPI	28	1	0.83279	0.00035	0.01	1616.8	9.8	0.1	14.7	0.00	1483.2	4.3	17.2

PPI	28	2	0.83279	0.00035	0.01	1200.0	6.9	0.1	14.5	0.06	1105.5	5.8	15.9
ER	1	1	0.83088	0.00034	0.06	1559.3	16.2	0.1	22.8	0.00	1370.6	4.7	26.9
ER	2	1	0.83088	0.00034	0.02	1434.8	9.3	0.1	15.9	0.00	1219.7	5.3	17.8
ER	2	2	0.83088	0.00034	0.11	1375.0	9.7	0.1	13.8	0.03	1279.7	5.0	16.6
ER	3	3	0.83088	0.00034	0.00	1173.7	32.3	0.0	63.7	-0.05	976.2	6.6	69.3
ER	4	1	0.83088	0.00034	0.23	798.1	9.9	0.2	20.9	-0.06	867.3	7.4	23.6
ER	4	2	0.83088	0.00034	0.43	689.2	17.3	0.4	20.6	-0.09	1002.0	6.4	32.7
ER	5	1	0.83088	0.00034	0.43	1047.4	13.4	0.4	10.4	-0.03	1524.5	4.2	22.3
ER	5	2	0.83088	0.00034	0.57	597.3	9.4	0.5	9.3	0.55	1154.1	5.6	20.7
ER	6	1	0.83088	0.00034	0.80	176.9	4.4	0.7	6.9	-0.04	732.9	8.8	19.6
ER	7	1	0.83088	0.00034	0.23	1125.6	10.0	0.2	10.9	-0.05	1213.8	5.3	15.4
ER	7	2	0.83088	0.00034	0.06	1303.4	9.8	0.1	33.3	0.04	1149.8	5.6	34.4
ER	8	1	0.83088	0.00017	0.27	1072.9	7.5	0.3	8.0	-0.18	1125.6	5.7	11.2
ER	9	1	0.83088	0.00017	0.43	1029.6	8.2	0.4	6.8	0.01	1386.6	4.6	13.0
ER	10	1	0.83088	0.00017	0.25	947.2	9.9	0.2	11.1	0.07	972.7	6.6	15.1
ER	11	1	0.83088	0.00017	0.02	1619.6	8.3	0.1	15.6	-0.01	1267.7	5.1	16.9
ER	12	1	0.83088	0.00017	0.03	1777.6	8.6	0.1	16.0	0.00	1401.3	4.6	17.4
ER	13	1	0.83088	0.00017	0.43	905.1	7.4	0.4	6.2	-0.03	1226.2	5.3	11.8
ER	13	2	0.83088	0.00017	0.01	1524.3	10.8	0.1	19.1	-0.01	1190.9	5.4	20.9
ER	14	1	0.83088	0.00017	0.33	1128.7	10.2	0.3	7.6	0.01	1296.3	5.0	14.0
ER	15	1	0.83088	0.00017	0.00	1668.4	5.4	0.0	9.5	0.00	1286.3	5.0	10.4
ER	15	2	0.83088	0.00017	0.04	1537.3	7.7	0.1	13.7	-0.01	1236.5	5.2	15.0
ER	16	1	0.83088	0.00017	0.04	1494.0	7.4	0.1	13.4	0.02	1192.3	5.4	14.6
ER	17	1	0.83088	0.00017	0.06	1345.9	11.1	0.1	20.0	0.00	1103.1	5.8	22.0
ER	18	1	0.83088	0.00017	0.18	1426.4	7.7	0.2	10.8	-0.02	1340.9	4.8	13.0
ER	19	1	0.83088	0.00017	0.35	1036.7	9.9	0.3	13.1	-0.04	1225.3	5.3	17.6
ER	20	1	0.83088	0.00017	0.02	1525.0	8.3	0.1	16.9	0.10	1199.6	5.4	18.1
ER	21	1	0.83088	0.00017	0.08	1460.4	4.1	0.1	7.8	-0.02	1227.0	5.3	8.6
ER	22	1	0.83088	0.00017	0.00	1610.7	13.8	0.0	25.6	0.00	1226.5	5.3	27.6
ER	23	1	0.83088	0.00017	0.04	1500.3	5.1	0.1	7.4	0.01	1208.1	5.3	8.4
ER	24	1	0.83088	0.00017	0.06	1267.6	9.3	0.1	16.3	0.01	1042.4	6.2	18.0
ER	25	1	0.83088	0.00017	0.05	1085.1	6.5	0.1	10.1	-0.01	884.0	7.3	11.4
ER	26	1	0.83088	0.00017	0.36	1023.9	9.3	0.3	12.5	-0.08	1237.2	5.2	16.8
ER	27	1	0.83088	0.00017	0.26	1381.1	10.0	0.3	8.4	0.00	1435.2	4.5	13.4
ER	28	1	0.83088	0.00017	0.18	1194.7	6.1	0.2	8.3	-0.04	1126.5	5.7	10.1
ER	29	1	0.83088	0.00017	0.22	624.7	7.1	0.2	9.1	-0.08	617.4	10.4	11.5
MBA	1	1	0.83541	0.00036	0.47	1416.6	11.7	0.4	14.7	-0.03	2191.5	2.9	23.5
MBA	1	2	0.83541	0.00036	0.08	2959.2	16.7	0.1	27.0	-0.66	2620.0	2.5	30.8
MBA	2	1	0.83541	0.00036	0.32	1786.4	15.3	0.3	20.0	-0.01	2162.7	3.0	27.3
MBA	2	2	0.83541	0.00036	0.05	3437.1	25.1	0.1	34.5	-0.01	2954.4	2.2	40.8
MBA	3	1	0.83541	0.00036	0.82	794.0	10.0	0.7	15.6	-0.03	3629.2	1.8	48.9
MBA	4	1	0.83541	0.00036	0.04	3159.1	14.5	0.1	26.5	-0.01	2695.7	2.4	29.3
MBA	5	1	0.83541	0.00036	0.07	2790.9	15.3	0.1	26.2	0.03	2469.2	2.6	29.6
MBA	6	1	0.83541	0.00036	0.06	2859.4	17.8	0.1	40.0	0.01	2501.9	2.6	43.0

MBA	7	1	0.83541	0.00036	0.16	2528.6	12.8	0.2	22.9	-0.02	2470.8	2.6	26.2
MBA	8	1	0.83541	0.00036	0.11	2716.5	16.0	0.1	30.2	-0.03	2498.1	2.6	33.7
MBA	8	2	0.83541	0.00036	0.01	3265.7	12.9	0.1	23.1	0.00	2708.0	2.4	25.5

MetaData			**206Pb/238U Age Summary***		
Date	Standard		ID-TIMS Offset %	Age (Ma)	Age 2s %
2072023	94-35		8.20	50.95	11.64
2072023	Fish Canyon		5.94	26.79	10.66
2072023	Plesovice		4.36	322.41	4.60
2072023	R33		4.56	400.19	5.40
2242023		91500	0.72	1070.09	5.31
2242023	94-35		0.94	54.98	17.61
2242023	FC1		0.16	1097.79	4.75
2242023	Fish Canyon		5.90	30.16	12.71
2242023	Plesovice		5.27	319.33	6.67
2242023	R33		4.56	400.19	5.95
3162023	Fish Canyon		0.46	28.61	15.40
3162023	Plesovice		2.60	345.85	4.78
4112023		91500	0.46	1067.30	4.29
4112023	94-35		2.10	54.33	11.43
4112024	Fish Canyon		1.01	28.19	15.40
5242023		91500	0.08	1063.24	3.94
5242023	94-35		1.01	56.06	13.91
5242023	Fish Canyon		0.41	28.36	10.92

	Accepted Age (Ma	2s (Ma)
94-35	55.5	0.08
Fish Canyon	28.478	0.024
Plesovice	337.1	0.2
R33	419.3	0.4
91500	1062.4	1.9
FC1	1099.5	0.33

Metadata			Data used for Correction of Isotope Ratios			Measured Isotope Ratios					Corrected 238U/206Pb Ratios & Age		
Unit	Crystal	Spot Number	Common 207Pb/206Pb	Common 207Pb/206Pb 2s	fraction Pb_c	238U/206Pb	238U/206Pb 2s %	207Pb/206Pb	207Pb/206Pb 2s %	rho	238U/206Pb c	206Pb/238U Age (Ma)	206Pb/238U Age 2s %
PPI	1	1	0.83279	0.00035	0.06	1469.7	8.0	0.1	13.0	-0.01	1411.5	4.6	15.2
PPI	1	2	0.83279	0.00035	0.05	1614.0	15.3	0.1	23.6	0.00	1532.1	4.2	27.8
PPI	2	1	0.83279	0.00035	0.31	758.6	6.5	0.3	9.8	-0.03	1003.3	6.4	13.0
PPI	2	2	0.83279	0.00035	0.20	1198.7	17.4	0.2	27.6	-0.13	1360.9	4.7	34.0
PPI	4	1	0.83279	0.00035	0.12	1585.1	28.6	0.1	45.1	-0.07	1622.2	4.0	53.9
PPI	4	2	0.83279	0.00035	0.11	1425.5	18.4	0.1	25.3	-0.02	1448.6	4.4	31.6
PPI	5	1	0.83279	0.00035	0.09	1388.6	6.7	0.1	10.4	0.00	1381.3	4.7	12.4
PPI	5	2	0.83279	0.00035	0.11	1337.5	7.0	0.1	11.0	-0.01	1356.7	4.7	13.2
PPI	5	3	0.83279	0.00035	0.08	1471.8	5.7	0.1	9.9	0.00	1448.4	4.4	11.4
PPI	6	1	0.83279	0.00035	0.08	1381.6	7.8	0.1	12.5	0.00	1364.7	4.7	14.7
PPI	6	2	0.83279	0.00035	0.05	1331.8	8.1	0.1	13.8	0.00	1271.9	5.1	15.8
PPI	7	1	0.83279	0.00035	0.05	1290.3	5.4	0.1	9.9	0.00	1225.5	5.3	11.2
PPI	7	2	0.83279	0.00035	0.30	966.2	11.8	0.3	13.5	0.26	1251.9	5.1	20.4
PPI	8	1	0.83279	0.00035	0.13	984.0	10.4	0.2	16.3	-0.26	1031.7	6.2	19.7
PPI	8	2	0.83279	0.00035	0.03	1426.4	12.0	0.1	21.2	-0.01	1336.9	4.8	24.1
PPI	11	1	0.83279	0.00035	0.06	1505.4	8.1	0.1	11.3	0.00	1449.4	4.4	13.8
PPI	11	2	0.83279	0.00035	0.11	1377.1	5.9	0.1	8.3	0.00	1402.3	4.6	10.3
PPI	12	1	0.83279	0.00035	0.03	1286.4	4.7	0.1	9.0	0.00	1208.0	5.3	10.1
PPI	12	2	0.83279	0.00035	0.03	1124.3	8.2	0.1	16.5	-0.04	1049.4	6.1	18.3
PPI	13	1	0.83279	0.00035	0.03	1276.1	7.9	0.1	14.4	0.00	1193.7	5.4	16.2
PPI	13	2	0.83279	0.00035	0.26	1155.9	7.0	0.3	8.7	0.03	1415.0	4.6	12.3
PPI	14	1	0.83279	0.00035	0.16	1016.4	14.9	0.2	20.9	0.02	1094.7	5.9	26.4
PPI	15	1	0.83279	0.00035	0.03	1310.7	7.1	0.1	14.6	-0.02	1228.8	5.2	16.0
PPI	15	2	0.83279	0.00035	0.18	1295.8	11.7	0.2	18.2	0.02	1437.1	4.5	22.5
PPI	16	1	0.83279	0.00035	0.05	1330.7	7.8	0.1	13.1	0.00	1264.2	5.1	15.1
PPI	16	2	0.83279	0.00035	0.04	1365.6	6.9	0.1	12.4	0.00	1289.8	5.0	14.0
PPI	17	1	0.83279	0.00035	0.08	1299.1	8.2	0.1	14.6	0.05	1274.8	5.1	16.7
PPI	18	1	0.83279	0.00035	0.06	1287.8	6.6	0.1	13.4	0.00	1242.2	5.2	14.9
PPI	19	2	0.83279	0.00035	0.15	1231.0	20.7	0.2	32.8	-88.32	1313.3	4.9	39.6
PPI	20	1	0.83279	0.00035	0.04	1388.0	6.0	0.1	11.4	0.00	1304.3	4.9	12.7
PPI	20	2	0.83279	0.00035	0.04	1507.1	10.7	0.1	18.8	0.00	1422.2	4.5	21.4
PPI	22	2	0.83279	0.00035	0.05	1084.8	6.4	0.1	12.0	0.00	1034.7	6.2	13.5
PPI	23	1	0.83279	0.00035	0.04	1137.1	19.8	0.1	32.7	0.58	1071.8	6.0	37.7
PPI	23	2	0.83279	0.00035	0.09	999.8	17.5	0.1	21.5	0.03	998.2	6.5	27.8
PPI	25	1	0.83279	0.00035	0.03	805.5	5.9	0.1	10.2	0.00	760.6	8.5	11.7
PPI	25	2	0.83279	0.00035	0.03	836.5	5.4	0.1	10.5	0.00	787.7	8.2	11.7
PPI	26	1	0.83279	0.00035	0.05	1287.8	4.8	0.1	9.3	0.01	1233.6	5.2	10.4
PPI	26	2	0.83279	0.00035	0.04	1290.4	3.1	0.1	5.7	0.00	1216.0	5.3	6.4
PPI	28	1	0.83279	0.00035	0.05	1616.8	9.8	0.1	13.4	0.00	1535.1	4.2	16.4

PPI	28	2	0.83279	0.00035	0.05	1200.0	6.9	0.1	14.3	0.06	1140.8	5.6	15.7
ER	1	1	0.83088	0.00034	0.09	1559.3	16.2	0.1	19.0	0.00	1423.6	4.5	24.2
ER	2	1	0.83088	0.00034	0.06	1434.8	9.3	0.1	16.1	0.00	1267.5	5.1	18.1
ER	2	2	0.83088	0.00034	0.17	1375.0	9.7	0.2	12.9	0.03	1378.9	4.7	16.3
ER	3	1	0.83088	0.00034	0.02	1173.7	32.3	0.1	64.6	-0.05	1000.1	6.4	70.4
ER	4	1	0.83088	0.00034	0.39	798.1	9.9	0.3	14.8	-0.06	1082.7	6.0	20.0
ER	4	2	0.83088	0.00034	0.66	689.2	17.3	0.6	20.4	-0.09	1657.0	3.9	46.6
ER	5	1	0.83088	0.00034	0.60	1047.4	13.4	0.5	9.5	-0.03	2153.8	3.0	29.5
ER	5	2	0.83088	0.00034	0.79	597.3	9.4	0.7	8.8	0.55	2330.1	2.8	38.2
ER	7	1	0.83088	0.00034	0.35	1125.6	10.0	0.3	10.1	-0.05	1430.2	4.5	16.4
ER	7	2	0.83088	0.00034	0.11	1303.4	9.8	0.1	16.4	0.04	1220.7	5.3	18.8
ER	8	1	0.83088	0.00034	0.29	1072.9	7.5	0.3	7.1	-0.18	1159.1	5.6	10.8
ER	9	1	0.83088	0.00034	0.45	1029.6	8.2	0.4	6.1	0.01	1424.3	4.5	12.9
ER	10	1	0.83088	0.00034	0.26	947.2	9.9	0.2	10.5	0.07	984.3	6.5	14.7
ER	11	1	0.83088	0.00034	0.02	1619.6	8.3	0.1	14.7	-0.01	1271.6	5.1	16.1
ER	12	1	0.83088	0.00034	0.03	1777.6	8.6	0.1	14.4	0.00	1403.9	4.6	15.9
ER	13	1	0.83088	0.00034	0.44	905.1	7.4	0.4	6.4	-0.03	1243.6	5.2	12.0
ER	13	2	0.83088	0.00034	0.02	1524.3	10.8	0.1	19.5	-0.01	1196.4	5.4	21.3
ER	14	1	0.83088	0.00034	0.35	1128.7	10.2	0.3	6.9	0.01	1328.8	4.8	13.9
ER	15	1	0.83088	0.00034	0.01	1668.4	5.4	0.1	10.0	0.00	1294.4	5.0	10.9
ER	15	2	0.83088	0.00034	0.04	1537.3	7.7	0.1	11.2	-0.01	1231.8	5.2	12.8
ER	16	1	0.83088	0.00034	0.04	1494.0	7.4	0.1	11.2	0.02	1201.6	5.4	12.6
ER	17	1	0.83088	0.00034	0.06	1345.9	11.1	0.1	19.1	0.00	1108.5	5.8	21.2
ER	18	1	0.83088	0.00034	0.19	1426.4	7.7	0.2	7.4	-0.02	1357.0	4.7	10.4
ER	19	1	0.83088	0.00034	0.34	1036.7	9.9	0.3	11.2	-0.04	1215.2	5.3	16.2
ER	20	1	0.83088	0.00034	0.02	1525.0	8.3	0.1	15.8	0.10	1201.2	5.4	17.1
ER	21	1	0.83088	0.00034	0.07	1460.4	4.1	0.1	5.6	-0.02	1211.2	5.3	6.6
ER	22	1	0.83088	0.00034	0.00	1610.7	13.8	0.0	28.0	0.00	1232.6	5.2	29.9
ER	23	1	0.83088	0.00034	0.05	1500.3	5.1	0.1	7.0	0.01	1215.7	5.3	8.1
ER	24	1	0.83088	0.00034	0.07	1267.6	9.3	0.1	16.2	0.01	1048.3	6.1	17.9
ER	25	1	0.83088	0.00034	0.05	1085.1	6.5	0.1	8.9	-0.01	886.1	7.3	10.4
ER	26	1	0.83088	0.00034	0.34	1023.9	9.3	0.3	9.8	-0.08	1198.5	5.4	14.6
ER	27	1	0.83088	0.00034	0.26	1381.1	10.0	0.3	7.9	0.00	1437.8	4.5	13.1
ER	28	1	0.83088	0.00034	0.19	1194.7	6.1	0.2	7.3	-0.04	1142.4	5.6	9.3
ER	29	1	0.83088	0.00034	0.22	624.7	7.1	0.2	8.0	-0.08	622.5	10.3	10.7
MBA	1	1	0.83541	0.00036	0.59	1416.6	11.7	0.5	13.1	-0.03	2803.0	2.3	26.8
MBA	1	2	0.83541	0.00036	0.12	2959.2	16.7	0.1	25.9	-0.66	2744.6	2.3	30.3
MBA	2	1	0.83541	0.00036	0.41	1786.4	15.3	0.4	16.8	-0.01	2484.7	2.6	27.2
MBA	2	2	0.83541	0.00036	0.08	3437.1	25.1	0.1	34.3	-0.01	3047.2	2.1	41.0
MBA	4	1	0.83541	0.00036	0.05	3159.1	14.5	0.1	22.2	-0.01	2730.2	2.4	25.6
MBA	5	1	0.83541	0.00036	0.09	2790.9	15.3	0.1	23.5	0.03	2509.0	2.6	27.3
MBA	6	1	0.83541	0.00036	0.07	2859.4	17.8	0.1	32.6	0.01	2519.4	2.6	36.2
MBA	7	1	0.83541	0.00036	0.21	2528.6	12.8	0.2	18.1	-0.02	2623.4	2.5	22.5
MBA	8	1	0.83541	0.00036	0.13	2716.5	16.0	0.1	23.8	-0.03	2553.1	2.5	28.3

MBA	8	2	0.83541	0.00036	0.04	3265.7	12.9	0.1	22.8	0.00	2769.3	2.3	25.3

Metadata			Data used for Correction of Isotope Ratios			Measured Isotope Ratios					Corrected 238U/206Pb Ratios & Age		
Unit	Crystal	Spot Number	Common 207Pb/206Pb	Common 207Pb/206Pb 2s	fraction Pb_c	238U/206Pb	238U/206Pb 2s %	207Pb/206Pb	207Pb/206Pb 2s %	rho	238U/206Pb c	206Pb/238U Age (Ma)	206Pb/238U Age 2s %
PPI	1	1	0.83279	0.00035	0.20	1469.7	8.0	0.2	10.5	-0.01	1667.1	3.9	13.9
PPI	1	2	0.83279	0.00035	0.07	1614.0	15.3	0.1	14.7	0.00	1569.7	4.1	21.0
PPI	2	1	0.83279	0.00035	0.21	758.6	6.5	0.2	11.4	-0.03	877.6	7.3	13.6
PPI	2	2	0.83279	0.00035	0.21	1198.7	17.4	0.2	20.2	-0.13	1374.9	4.7	28.5
PPI	4	1	0.83279	0.00035	0.16	1585.1	28.6	0.2	21.0	-0.07	1702.8	3.8	37.4
PPI	4	2	0.83279	0.00035	0.22	1425.5	18.4	0.2	10.2	-0.02	1646.8	3.9	23.8
PPI	5	1	0.83279	0.00035	0.06	1388.6	6.7	0.1	8.7	0.00	1335.2	4.8	10.8
PPI	5	2	0.83279	0.00035	0.07	1337.5	7.0	0.1	8.6	-0.01	1305.0	4.9	11.0
PPI	5	3	0.83279	0.00035	0.16	1471.8	5.7	0.2	10.3	0.00	1588.9	4.1	12.0
PPI	6	1	0.83279	0.00035	0.07	1381.6	7.8	0.1	9.3	0.00	1338.9	4.8	12.0
PPI	6	2	0.83279	0.00035	0.02	1331.8	8.1	0.1	11.5	0.00	1229.1	5.2	13.7
PPI	7	1	0.83279	0.00035	0.02	1290.3	5.4	0.1	8.1	0.00	1188.2	5.4	9.5
PPI	7	2	0.83279	0.00035	0.38	966.2	11.8	0.3	11.7	0.26	1409.3	4.6	20.9
PPI	8	1	0.83279	0.00035	0.13	984.0	10.4	0.1	11.9	-0.26	1024.8	6.3	16.2
PPI	8	2	0.83279	0.00035	0.04	1426.4	12.0	0.1	12.2	-0.01	1348.6	4.8	16.7
PPI	11	1	0.83279	0.00035	0.04	1505.4	8.1	0.1	8.8	0.00	1412.5	4.6	11.6
PPI	11	2	0.83279	0.00035	0.07	1377.1	5.9	0.1	7.7	0.00	1333.8	4.8	9.6
PPI	12	1	0.83279	0.00035	0.01	1286.4	4.7	0.1	8.0	0.00	1177.2	5.5	9.1
PPI	12	2	0.83279	0.00035	0.03	1124.3	8.2	0.1	9.8	-0.04	1049.0	6.1	12.5
PPI	13	1	0.83279	0.00035	0.02	1276.1	7.9	0.1	9.3	0.00	1177.1	5.5	11.8
PPI	13	2	0.83279	0.00035	0.16	1155.9	7.0	0.2	9.3	0.03	1247.6	5.2	12.1
PPI	14	1	0.83279	0.00035	0.18	1016.4	14.9	0.2	14.7	0.02	1127.8	5.7	22.2
PPI	15	1	0.83279	0.00035	0.02	1310.7	7.1	0.1	10.5	-0.02	1213.1	5.3	12.4
PPI	15	2	0.83279	0.00035	0.80	1295.8	11.7	0.7	12.9	0.02	5664.5	1.1	53.2
PPI	16	1	0.83279	0.00035	0.03	1330.7	7.8	0.1	9.1	0.00	1240.1	5.2	11.7
PPI	16	2	0.83279	0.00035	0.02	1365.6	6.9	0.1	9.3	0.00	1262.5	5.1	11.3
PPI	17	1	0.83279	0.00035	0.26	1299.1	8.2	0.2	10.4	0.05	1579.1	4.1	14.5
PPI	18	1	0.83279	0.00035	0.03	1287.8	6.6	0.1	10.0	0.00	1206.9	5.3	11.8
PPI	19	2	0.83279	0.00035	0.24	1231.0	20.7	0.2	17.5	-88.32	1466.7	4.4	30.4
PPI	20	1	0.83279	0.00035	0.01	1388.0	6.0	0.1	9.4	0.00	1271.2	5.1	10.9
PPI	20	2	0.83279	0.00035	0.01	1507.1	10.7	0.1	13.4	0.00	1380.1	4.7	16.6
PPI	22	2	0.83279	0.00035	0.03	1084.8	6.4	0.1	9.4	0.00	1013.7	6.4	11.1
PPI	23	1	0.83279	0.00035	0.06	1137.1	19.8	0.1	15.2	0.58	1100.3	5.9	24.6
PPI	23	2	0.83279	0.00035	0.12	999.8	17.5	0.1	16.6	0.03	1028.2	6.3	24.6
PPI	25	1	0.83279	0.00035	0.00	805.5	5.9	0.1	9.6	0.00	738.0	8.7	11.1
PPI	25	2	0.83279	0.00035	0.01	836.5	5.4	0.1	8.4	0.00	769.1	8.4	9.8
PPI	26	1	0.83279	0.00035	0.02	1287.8	4.8	0.1	8.0	0.01	1191.5	5.4	9.2
PPI	26	2	0.83279	0.00035	0.01	1290.4	3.1	0.1	5.3	0.00	1177.0	5.5	6.1
PPI	28	1	0.83279	0.00035	0.04	1616.8	9.8	0.1	9.3	0.00	1519.4	4.2	13.1

PPI	28	2	0.83279	0.00035	0.03	1200.0	6.9	0.1	9.8	0.06	1127.5	5.7	11.8
ER	1	1	0.83088	0.00034	0.13	1559.3	16.2	0.1	11.3	0.00	1482.6	4.3	19.2
ER	2	1	0.83088	0.00034	0.05	1434.8	9.3	0.1	10.4	0.00	1250.2	5.2	13.3
ER	2	2	0.83088	0.00034	0.14	1375.0	9.7	0.2	10.1	0.03	1328.8	4.8	13.8
ER	3	3	0.83088	0.00034	0.08	1173.7	32.3	0.1	18.4	-0.05	1067.3	6.0	34.9
ER	4	1	0.83088	0.00034	0.26	798.1	9.9	0.3	16.7	-0.06	905.8	7.1	20.2
ER	4	2	0.83088	0.00034	0.45	689.2	17.3	0.4	18.1	-0.09	1042.9	6.2	32.0
ER	5	1	0.83088	0.00034	0.46	1047.4	13.4	0.4	9.3	-0.03	1594.9	4.0	22.7
ER	5	2	0.83088	0.00034	0.59	597.3	9.4	0.5	8.7	0.55	1201.9	5.4	21.1
ER	6	1	0.83088	0.00034	0.80	176.9	4.4	0.7	6.9	-0.04	733.8	8.8	19.7
ER	7	1	0.83088	0.00034	0.24	1125.6	10.0	0.2	9.9	-0.05	1232.7	5.2	14.9
ER	7	2	0.83088	0.00034	0.20	1303.4	9.8	0.2	11.5	0.04	1353.4	4.8	15.4
ER	8	1	0.83088	0.00034	0.27	1072.9	7.5	0.3	7.8	-0.18	1127.7	5.7	11.1
ER	9	1	0.83088	0.00034	0.43	1029.6	8.2	0.4	6.7	0.01	1383.5	4.7	12.9
ER	10	1	0.83088	0.00034	0.26	947.2	9.9	0.2	10.0	0.07	986.4	6.5	14.3
ER	11	1	0.83088	0.00034	0.04	1619.6	8.3	0.1	9.0	-0.01	1301.8	4.9	11.2
ER	12	1	0.83088	0.00034	0.07	1777.6	8.6	0.1	7.9	0.00	1466.1	4.4	10.6
ER	13	1	0.83088	0.00034	0.44	905.1	7.4	0.4	6.0	-0.03	1235.7	5.2	11.8
ER	13	2	0.83088	0.00034	0.04	1524.3	10.8	0.1	11.6	-0.01	1216.6	5.3	14.5
ER	14	1	0.83088	0.00034	0.34	1128.7	10.2	0.3	7.1	0.01	1306.4	4.9	13.8
ER	15	1	0.83088	0.00034	0.01	1668.4	5.4	0.1	7.0	0.00	1298.0	5.0	8.1
ER	15	2	0.83088	0.00034	0.08	1537.3	7.7	0.1	7.9	-0.01	1283.2	5.0	10.2
ER	16	1	0.83088	0.00034	0.06	1494.0	7.4	0.1	8.8	0.02	1219.2	5.3	10.7
ER	17	1	0.83088	0.00034	0.08	1345.9	11.1	0.1	14.7	0.00	1123.2	5.7	17.4
ER	18	1	0.83088	0.00034	0.20	1426.4	7.7	0.2	9.1	-0.02	1366.7	4.7	11.7
ER	19	1	0.83088	0.00034	0.37	1036.7	9.9	0.3	11.2	-0.04	1270.6	5.1	16.5
ER	20	1	0.83088	0.00034	0.07	1525.0	8.3	0.1	7.9	0.10	1258.9	5.1	10.4
ER	21	1	0.83088	0.00034	0.10	1460.4	4.1	0.1	6.4	-0.02	1243.1	5.2	7.3
ER	22	1	0.83088	0.00034	0.01	1610.7	13.8	0.1	13.5	0.00	1251.3	5.1	17.3
ER	23	1	0.83088	0.00034	0.05	1500.3	5.1	0.1	6.1	0.01	1216.3	5.3	7.4
ER	24	1	0.83088	0.00034	0.12	1267.6	9.3	0.1	8.2	0.01	1112.2	5.8	11.6
ER	25	1	0.83088	0.00034	0.06	1085.1	6.5	0.1	7.8	-0.01	896.2	7.2	9.5
ER	26	1	0.83088	0.00034	0.42	1023.9	9.3	0.4	9.3	-0.08	1363.5	4.7	15.5
ER	27	1	0.83088	0.00034	0.28	1381.1	10.0	0.3	7.2	0.00	1472.6	4.4	12.9
ER	28	1	0.83088	0.00034	0.18	1194.7	6.1	0.2	8.0	-0.04	1122.6	5.7	9.8
ER	29	1	0.83088	0.00034	0.22	624.7	7.1	0.2	8.2	-0.08	623.7	10.3	10.9
MBA	1	1	0.83541	0.00036	0.59	1416.6	11.7	0.5	10.4	-0.03	2817.6	2.3	25.8
MBA	1	2	0.83541	0.00036	0.19	2959.2	16.7	0.2	11.7	-0.66	2966.3	2.2	20.6
MBA	2	1	0.83541	0.00036	0.48	1786.4	15.3	0.4	11.6	-0.01	2809.3	2.3	26.9
MBA	2	2	0.83541	0.00036	0.19	3437.1	25.1	0.2	11.9	-0.01	3424.7	1.9	27.9
MBA	4	1	0.83541	0.00036	0.13	3159.1	14.5	0.1	11.3	-0.01	2954.9	2.2	17.8
MBA	5	1	0.83541	0.00036	0.18	2790.9	15.3	0.2	11.7	0.03	2772.1	2.3	19.3
MBA	6	1	0.83541	0.00036	0.23	2859.4	17.8	0.2	12.9	0.01	3029.9	2.1	23.0
MBA	7	1	0.83541	0.00036	0.30	2528.6	12.8	0.3	11.5	-0.02	2931.1	2.2	18.9

MBA	8	1	0.83541	0.00036	0.28	2716.5	16.0	0.3	11.6	-0.03	3080.2	2.1	21.7
MBA	8	2	0.83541	0.00036	0.06	3265.7	12.9	0.1	11.3	0.00	2839.9	2.3	16.0

*dh: Downhole

Metadata			Data used for Correction of Isotope Ratios		Measured Isotope Ratios					Concordant 238U/206Pb Ratios & Age		
Unit	Crystal	Spot Number*	Common 207Pb/206Pb	Common 207Pb/206Pb 2s	238U/206Pb	238U/206Pb 2	207Pb/206Pb	207Pb/206Pb 2s %	rho	238U/206Pb	206Pb/238U Age	206Pb/238U Age 2s %
PPI	1	1	0.83279	0.00035	393.4	1.7	0.5	7.9	-0.05	1384.9	4.7	9.8
PPI	1	1-dh	0.83279	0.00035	570.5	1.0	0.2	8.4	0.00	1124.0	5.8	8.6
PPI	2	1	0.83279	0.00035	725.2	1.7	0.1	16.6	-0.03	1121.3	5.8	16.9
PPI	3	1	0.83279	0.00035	777.6	0.8	0.1	15.1	0.00	1170.0	5.6	15.2
PPI	4	1	0.83279	0.00035	428.6	1.6	0.4	9.1	-0.06	1078.3	6.0	10.5
PPI	5	1	0.83279	0.00035	702.7	0.5	0.1	11.2	-0.01	1094.9	6.0	11.3
PPI	5	2	0.83279	0.00035	727.8	0.7	0.0	15.3	0.00	1075.4	6.1	15.3
PPI	6	1	0.83279	0.00035	728.9	0.9	0.1	11.9	-0.01	1121.6	5.8	12.0
PPI	6	2	0.83279	0.00035	624.6	3.2	0.2	19.5	-0.01	1144.9	5.7	20.4
PPI	7	1	0.83279	0.00035	535.0	0.5	0.1	10.0	-0.04	835.9	7.8	10.0
PPI	7	2	0.83279	0.00035	484.5	0.6	0.1	8.0	0.00	719.4	9.0	8.0
PPI	8	1	0.83279	0.00035	740.9	0.4	0.1	8.7	0.00	1103.8	5.9	8.7
PPI	8	2	0.83279	0.00035	742.9	0.5	0.1	11.4	0.00	1110.3	5.9	11.4
PPI	8	3	0.83279	0.00035	769.5	0.6	0.1	8.9	0.00	1185.8	5.5	9.0
PPI	9	1	0.83279	0.00035	445.8	2.1	0.2	11.1	-0.07	883.0	7.4	12.0
PPI	9	1-dh	0.83279	0.00035	460.1	0.9	0.2	8.8	-0.03	854.9	7.6	9.0
PPI	9	2	0.83279	0.00035	568.3	1.1	0.1	11.6	-0.05	917.7	7.1	11.8
PPI	10	1	0.83279	0.00035	492.7	1.7	0.4	8.9	-0.07	1285.8	5.1	9.9
PPI	10	2	0.83279	0.00035	780.6	0.8	0.1	14.6	-0.01	1189.3	5.5	14.7
PPI	10	2-dh	0.83279	0.00035	354.6	1.5	0.5	7.6	-0.06	1218.1	5.4	9.2
PPI	11	1	0.83279	0.00035	744.5	0.3	0.1	9.9	0.01	1154.8	5.7	10.0
PPI	11	2	0.83279	0.00035	692.0	0.5	0.1	10.2	-0.03	1119.4	5.8	10.3
PPI	12	1	0.83279	0.00035	739.4	1.1	0.1	21.1	0.01	1100.8	5.9	21.1
PPI	13	1	0.83279	0.00035	576.5	0.9	0.2	9.1	-0.05	1134.6	5.8	9.3
PPI	13	2	0.83279	0.00035	766.8	2.1	0.1	21.6	-0.01	1175.2	5.6	21.9
PPI	14	1	0.83279	0.00035	645.8	1.2	0.1	14.3	-0.03	1024.5	6.4	14.4
PPI	15	1	0.83279	0.00035	780.8	0.7	0.1	14.7	0.00	1161.6	5.6	14.8
PPI	15	2	0.83279	0.00035	762.4	0.5	0.0	12.4	0.00	1123.0	5.8	12.4
PPI	15	3	0.83279	0.00035	736.5	0.6	0.1	11.8	0.00	1138.8	5.7	11.9
PPI	16	1	0.83279	0.00035	486.1	5.5	0.4	12.8	-0.06	1265.9	5.2	18.1
PPI	16	2	0.83279	0.00035	771.6	0.7	0.1	13.7	0.01	1161.2	5.6	13.7
PPI	16	3	0.83279	0.00035	771.6	1.1	0.1	20.0	0.00	1163.7	5.6	20.1
ER	1	1	0.83088	0.00034	846.9	0.6	0.1	11.1	0.00	1254.9	5.2	11.1
ER	1	2	0.83088	0.00034	710.8	2.2	0.2	13.8	-0.05	1322.8	4.9	14.4
ER	1	2-dh	0.83088	0.00034	788.1	1.1	0.1	15.4	0.00	1229.7	5.3	15.5
ER	1	3	0.83088	0.00034	645.1	1.8	0.2	12.5	-0.05	1209.2	5.4	13.0
ER	1	3-dh	0.83088	0.00034	539.1	1.3	0.3	9.4	-0.03	1135.3	5.7	9.9
ER	2	1	0.83088	0.00034	622.6	0.7	0.4	6.9	-0.02	1672.9	3.9	7.2
ER	2	2	0.83088	0.00034	1019.6	1.2	0.1	17.5	-0.04	1604.1	4.1	17.7

ER	2	2-dh	0.83088	0.00034	923.5	1.3	0.1	15.0	-0.03	1472.3	4.5	15.1
ER	3	1	0.83088	0.00034	566.2	2.5	0.3	10.3	-0.05	1289.7	5.1	11.9
ER	3	2	0.83088	0.00034	626.3	2.0	0.3	10.5	-0.05	1326.7	4.9	11.5
ER	3	2-dh	0.83088	0.00034	293.7	4.3	0.6	8.2	-0.06	1439.5	4.5	21.7
MBA	1	1	0.83541	0.00036	1594.1	1.1	0.1	12.2	0.00	2652.8	2.5	12.4
MBA	1	2	0.83541	0.00036	1625.5	1.8	0.1	21.1	0.00	2665.9	2.5	21.2
MBA	2	1	0.83541	0.00036	1720.6	3.0	0.1	25.6	0.00	2837.3	2.3	25.9
MBA	3	1	0.83541	0.00036	1818.6	5.6	0.2	30.3	0.00	3345.2	2.0	31.6
MBA	4	1	0.83541	0.00036	1626.6	5.9	0.1	25.1	0.00	2743.7	2.4	26.1
MBA	4	2	0.83541	0.00036	1217.2	3.8	0.3	15.8	-0.02	2757.5	2.4	17.9
MBA	5	1	0.83541	0.00036	1486.4	1.5	0.2	14.0	0.00	2764.0	2.4	14.3
MBA	5	2	0.83541	0.00036	1533.2	2.1	0.1	17.8	0.01	2658.8	2.5	18.1
MBA	6	1	0.83541	0.00036	1548.3	3.3	0.1	22.3	0.01	2625.8	2.5	22.9
MBA	6	2	0.83541	0.00036	1486.3	2.7	0.2	17.5	0.00	2786.5	2.4	18.2
MBA	7	1	0.83541	0.00036	1313.0	2.8	0.2	16.8	0.00	2638.1	2.5	17.5
MBA	7	2	0.83541	0.00036	1554.6	2.8	0.1	19.8	0.01	2714.5	2.4	20.4
MBA	8	1	0.83541	0.00036	1770.8	4.5	0.1	26.6	0.00	2948.3	2.3	27.3
MBA	1	1	0.83541	0.00036	1291.1	8.3	0.2	30.0	-0.02	2723.5	2.4	38.1
MBA	2	1	0.83541	0.00036	1583.6	1.1	0.1	17.6	0.00	2523.4	2.6	17.7
MBA	2	1-dh	0.83541	0.00036	1534.2	1.4	0.1	25.3	0.00	2433.7	2.7	25.4
MBA	2	2	0.83541	0.00036	1409.1	5.0	0.2	18.6	0.00	2754.8	2.4	20.0
MBA	3	1	0.83541	0.00036	1640.1	1.5	0.1	22.0	-0.01	2641.8	2.5	22.2
MBA	3	1-dh	0.83541	0.00036	1454.6	2.6	0.1	23.6	-0.01	2350.7	2.8	23.9
MBA	3	2	0.83541	0.00036	1552.1	1.6	0.1	15.8	0.00	2707.2	2.5	16.1
MBA	4	1	0.83541	0.00036	1662.6	2.6	0.1	26.8	0.00	2825.6	2.4	27.2
MBA	4	1-dh	0.83541	0.00036	764.8	2.8	0.5	9.1	-0.02	2763.7	2.4	12.5
MBA	4	2	0.83541	0.00036	1617.3	5.0	0.1	28.4	0.01	2912.0	2.3	29.6
MBA	4	2-dh	0.83541	0.00036	1486.3	2.6	0.1	23.1	0.01	2496.0	2.7	23.5
MBA	4	3	0.83541	0.00036	1027.7	2.1	0.3	11.4	-0.01	2487.9	2.7	12.3
MBA	5	1	0.83541	0.00036	770.2	1.6	0.1	14.0	0.00	1321.7	4.9	14.3
MBA	5	1-dh	0.83541	0.00036	1018.9	3.0	0.1	18.3	-0.01	1710.3	3.8	19.0
MBA	6	1	0.83541	0.00036	1205.0	1.3	0.3	9.8	0.00	2562.8	2.6	10.2
MBA	7	1	0.83541	0.00036	1216.6	1.5	0.3	10.7	-0.03	2781.1	2.4	11.3
MBA	7	2	0.83541	0.00036	1565.3	1.2	0.1	14.1	0.00	2651.8	2.5	14.2
MBA	7	3	0.83541	0.00036	1545.6	1.6	0.1	17.3	0.00	2577.0	2.6	17.5
MBA	8	1	0.83541	0.00036	1416.6	1.8	0.1	17.8	0.00	2523.4	2.6	18.0
MBA	8	2	0.83541	0.00036	1241.9	3.2	0.3	14.2	-0.02	2823.9	2.4	16.1
MBA	9	1	0.83541	0.00036	1722.1	1.1	0.1	22.0	0.00	2755.3	2.4	22.1
MBA	9	1-dh	0.83541	0.00036	1315.3	1.6	0.2	12.2	-0.01	2590.6	2.6	12.6
MBA	9	2	0.83541	0.00036	1670.2	1.5	0.1	22.5	0.00	2687.5	2.5	22.6
MBA	9	2-dh	0.83541	0.00036	1482.1	1.8	0.1	17.4	0.00	2557.6	2.6	17.7
MBA	10	1	0.83541	0.00036	1175.7	2.7	0.2	16.1	-0.01	2409.0	2.7	17.1
MBA	10	2	0.83541	0.00036	1559.7	2.1	0.1	26.3	0.00	2458.2	2.7	26.5

MetaData			206Pb/238U Age Summary*		
Date	Run	Standard	ID-TIMS Offset %	Age (Ma)	Age 2s %
3202024	1	Temora	0.73	413.75	4.15
3202024	1	91500	1.81	1081.67	4.14
3202024	2	Temora	1.33	411.24	5.13
3202024	2	91500	1.61	1045.32	5.14
3212024	1	Temora	2.38	426.70	7.07
3212024	1	91500	0.12	1063.64	7.06
3212024	2	Temora	1.81	409.23	5.06
3212024	2	91500	0.42	1057.93	5.04
3222024	1	Temora	2.73	428.17	4.50
3222024	1	91500	0.15	1064.04	4.48
3222024	2	Temora	4.99	437.59	8.08
3222024	2	91500	0.69	1069.72	8.24

	Accepted Age (Ma	2s (Ma)
91500	1062.4	1.9
Temora	416.78	0.33

#Estimated with Stacey-Kramers model

Metadata				Data used for Correction of Isotope Ratios			Measured Isotope Ratios					Corrected 238U/206Pb Ratios & Age		
Unit	Crystal	Spot Number	Method	Common 207Pb/206Pb	Common 207Pb/206Pb 2s	fraction Pb_c	238U/206Pb	238U/206Pb 2s %	207Pb/206Pb	207Pb/206Pb 2s %	rho	238U/206Pb c	206Pb/238U Age (Ma)	206Pb/238U Age 2s %
CHX22_21.03_-_1	3	1	Q	0.86	0.05	0.01	17.6	2.9	0.1	3.1	0.06	16.3	383.7	9.5
CHX22_21.03_-_2	3	2	Q	0.87	0.05	0.00	13.7	2.7	0.1	3.1	0.06	12.7	489.5	9.4
CHX22_21.10_-_1	9	1	Q	0.85	0.05	0.01	42.1	3.3	0.1	3.3	0.06	39.1	162.6	9.6
CHX22_21.10_-_2	9	2	Q	0.84	0.05	0.00	269.7	4.0	0.0	6.8	0.05	248.2	25.9	11.9
CHX22_21.29_-_1	29	1	Q	0.87	0.05	0.00	12.5	2.3	0.1	3.5	0.06	11.5	535.4	9.5
CHX22_21.24_-_1	30	1	Q	0.98	0.07	0.01	3.1	2.3	0.1	2.2	0.12	2.9	1914.0	9.7
CHX22_21.24_-_2	30	2	Q	0.97	0.06	0.04	3.4	2.3	0.1	3.5	0.14	3.3	1706.6	10.1
CHX22-21TC-25	14	2	MC	0.88	0.05	0.01	9.3	0.6	0.1	0.2	0.78	14.0	443.6	10.9

LA-Q-ICP-MS Data							
Crystal	Age (Ma)	1s Age %	Length	Width	Aspect	CL Luminesence	Spot Location
1	4.6	7.6	413	106	0.256658596	Dark	Rim
	4.2	13.9				Gray	Core
2	6.4	6.5	318	72	0.226415094	Bright	Rim
	4.7	17.0				Gray	Core
3	383.7	4.3	198	142	0.717171717	Gray	Rim
	489.5	4.6				Gray	Core
4	4.0	26.9	280	151	0.539285714	Gray	Core
	4.4	15.8				Gray	Rim
5	4.7	6.2	258	138	0.534883721	Dark	Rim
	4.7	6.6				Bright	Core
	4.4	5.7				Gray	Core
6	4.7	7.4	211	81	0.383886256	Dark	Rim
	5.1	7.9				Gray	Core
7	5.3	5.6	181	78	0.430939227	Gray	Rim
	5.1	10.2				Gray	Core
8	6.2	9.8	252	86	0.341269841	Gray	Rim
	4.8	12.0				Gray	Core
9	25.9	6.0	315	110	0.349206349	Dark	Rim
	162.6	4.8				Bright	Core
11	4.4	6.9	153	101	0.660130719	Gray	Core
	4.6	5.1				Gray	Core
12	5.3	5.0	154	71	0.461038961	Gray	Rim
	6.1	9.1				Gray	Core
13	5.4	8.1	161	92	0.571428571	Gray	Rim
	4.6	6.1				Gray	Core
14	5.9	13.2	122	62	0.508196721	Gray	Rim
15	5.2	8.0	201	117	0.582089552	Dark	Rim
	4.5	11.2				Gray	Core
16	5.1	7.5	174	108	0.620689655	Gray	Rim
	5.0	7.0				Gray	Core
17	5.1	8.4	191	70	0.366492147	Gray	Core
18	5.2	7.4	118	86	0.728813559	Bright	Core
19	4.9	19.8	265	85	0.320754717	Bright	Core
20	4.9	6.4	164	65	0.396341463	Bad CL	Rim
	4.5	10.7				Bad CL	Core
22	6.2	6.8	140	81	0.578571429	Bright	Rim
23	6.0	18.9	94	43	0.457446809	Dark	Rim

	SIMS		LAICPMS		
	Old Age	No Old Age	Old Age	No Old Age	SIMS Non-Participants
Bright Core	0	15	3	3	7
Not Bright Core	2	33	7	32	48
Bright-Core Old Age Association	0			4.6	
Adjusted Odds	1.8				

LA-Q-ICP-MS CL-Images

	6.5	13.9				Gray	Core
25	8.5	5.8	130	58	0.446153846	Dark	Rim
	8.2	5.9				Gray	Core
26	5.2	5.2	167	76	0.45508982	Dark	Rim
	5.3	3.2				Dark	Core
28	4.2	8.2	213	89	0.417840376	Bright	Rim
	5.6	7.9				Gray	Core
29	535.4	4.8	116	84	0.724137931	Bright	Core
30	1914.0	4.9	123	80	0.650406504	Bright	Core
	1706.6	5.1				Gray	Rim
31	5.0	6.2	256	81	0.31640625	Bright	Core

SIMS Data									
Crystal	**Age (Ma)**	**1s Age %**	**Length**	**Width**	**Aspect**	**CL Luminescence**	**Spot Location**	**Non-Participant Spot**	**Non-Participatns Luminescence**
1	4.90	10.48	214.849	86.538	0.402785212	Bright	Core	Rim	Gray
2	4.53	10.17	171.467	65.115	0.379752372	Bright	Core	Rim	Dark
3	4.17	9.72	234.303	78.531	0.335168564	Gray	Core	Rim	Dark
								Core	Bright
4	7.56	6.77	130.775	71.467	0.546488243	Bright	Rim	Core	Bright
5	4.46	6.95	197.145	93.648	0.475020924	Gray	Core	Rim	Gray
6	4.42	5.59	140.389	55.543	0.39563641	Gray	Core	Rim	Dark
7	4.20	8.08	114.162	69.635	0.609966539	Dark	Core	Rim	Dark
8	4.65	7.94	356.073	57.245	0.160767595	Gray	Core	Core	Gray
								Rim	Dark
9	5.34	11.20	178.776	105.435	0.589760371	Gray	Core	Rim	Dark
10	4.06	9.34	444.072	72.602	0.163491506	Gray	Core	Rim	Dark
								Rim	Bright
11	4.95	8.39	475.88	78.259	0.164451122	Gray	Core	Rim	Dark
12	4.48	7.71	158.619	98.407	0.620398565	Bright	Core	Rim	Gray
13	5.11	12.10	351.141	105.109	0.299335595	Gray	Core	Rim	Dark
14	4.43	5.95	326.827	66.212	0.202590361	Dark	Rim	Core	Bright

15	5.61	6.58	198.04	42.19	0.21303777	Gray	Core	Rim	Gray
16	4.81	7.48	312.416	121.672	0.389455086	Gray	Core	Rim	Gray
17	4.27	9.22	140.911	56.356	0.399940388	Dark	Core	Rim	Dark
18	4.24	11.32	176.647	55.714	0.315397374	Dark	Core	Rim	Bright
19	4.84	12.01	271.183	64.125	0.236463938	Gray	Core	Rim	Dark
								Core	Gray
20	4.35	9.93	178.997	46.174	0.257959631	Gray	Core	Rim	Gray
21	4.20	13.44	531.88	89.554	0.168372565	Bright	Core	Rim	Dark
22	4.23	7.75	268.701	72.139	0.268473136	Bright	Core	Rim	Dark
23	4.19	10.72	96.602	59.666	0.617647668	Gray	Core	Rim	Gray
24	4.62	8.55	192.01	49.396	0.257257435	Bright	Core	Rim	Gray
25	4.71	8.45	115.741	75.153	0.649320466	Gray	Core	Rim	Dark
26	4.95	10.65	206.243	73.348	0.355638737	Gray	Core	Rim	Bright
								Rim	Gray
27	4.37	7.23	158.202	72.25	0.456694606	Gray	Core	Rim	Dark
28	4.26	13.07	160.86	75.073	0.46669775	Gray	Core	Rim	Dark
								Rim	Gray
29	4.72	9.07	194.01	46.861	0.241539096	Gray	Core	Core	Bright
								Rim	Dark
30	280.90	6.97	227.903	98.489	0.432153153	Dark	Core	Rim	Gray
31	4.32	10.19	217.807	50.99	0.234106342	Bright	Core	Rim	Dark
32	4.29	12.98	164.195	62.032	0.377794695	Gray	Core	Rim	Dark
33	4.34	9.67	162.542	70.228	0.432060637	Gray	Core	Rim	Gray
34	4.52	7.98	222.657	58.822	0.264182128	Gray	Core	Rim	Gray
35	4.16	8.88	233.324	93.723	0.401686067	Bright	Core	Rim	Gray
36	5.49	8.37	161.245	76.968	0.477335731	Bright	Core	Rim	Dark

SIMS CL-Images

37	4.49	12.23	153.154	96.208	).628178174	Bright	Core	Rim	Gray
38	4.38	9.63	194.659	86.579	).444772654	Gray	Core	Rim	Gray
39	4.35	8.84	161.914	69.857	).431445088	Bright	Core	Rim	Dark
40	4.46	9.52	196.163	72.691	).370564276	Gray	Core	Rim	Dark
41	4.46	13.28	228.281	74.967	).328397896	Gray	Core	Rim	Gray
42	4.58	6.58	182.395	58.138	).318747773	Bright	Rim	Core	Bright
43	4.43	8.75	219.389	70.717	).322336124	Bright	Core	Rim	Dark
44	4.25	9.07	248.387	68.261	0.27481712	Gray	Core	Rim	Dark
								Rim	Bright
45	4.97	15.23	251.834	72.16	).286537958	Gray	Rim	Core	Bright
46	4.78	11.17	117.068	83.533	).713542556	Bright	Core	Rim	Dark
47	4.62	9.69	186.424	92.875	).498192293	Gray	Core	Rim	Dark
48	4.81	11.89	134.138	66.024	).492209516	Bright	Core	Rim	Gray
49	4.43	10.51	241.643	75.2	0.31120289	Gray	Core	Rim	Dark
								Core	Bright
50	3.94	14.89	341.594	55.458	).162350627	Bright	Core	Rim	Dark

(Kern et al. 2016)

Sample	**Unit**	**207Pb/206Pt**	**207Pb/206Pb 2S**	**208Pb/204Pt**	**208Pb/204Pb 2S**	**207Pb/204Pt**	**207Pb/204Pb 2S**	**206Pb/204Pt**	**206Pb/204Pb 2S**	**208Pb/206Pt**	**208Pb/206Pb 2S**
CHX22-21	Puripicar	0.83279	0.00035	38.815	0.010	15.6684	0.0009	18.815	0.009	2.06299	0.00043
CHX22-15	Embaucador Rhyolite	0.83088	0.00034	38.848	0.009	15.6713	0.0006	18.862	0.009	2.05953	0.00044
CHX22-04	Middle B&A	0.83541	0.00036	38.832	0.012	15.6674	0.0011	18.753	0.010	2.07047	0.00039